Erasmus Mundus Master
in Astrophysics and Space Science

Master Thesis

Tracing Asymmetries in the 67P's Dust Coma Brightness Distribution Using Rosetta's OSIRIS Observations

Supervisors

Dr. Raphael Marshall
Côte d'Azur University, Côte d'Azur Observatory, Nice, France
International Space Science Institution, Bern, Switzerland

Dr. Cecilia Tubiana
INAF-IAPS, Institute of Astrophysics and Planetology, Rome, Italy

Prof. Alessandro Mura
INAF-IAPS, Institute of Astrophysics and Planetology, Rome, Italy
University Tor Vergata, Rome, Italy

Author

Daniella Glezina
Côte d'Azur University, Côte d'Azur Observatory, Nice, France
Universitá degli Studi di Roma Tor Vergata, Rome, Italy

Academic Year 2024/2025

This Master thesis is submitted in partial fulfillment of the requirements for the degree *Master Physique Fondamental et Applications, parcours MASS* as part of a multiple degree awarded in the framework of the Erasmus Mundus Joint Master in Astrophysics and Space Science – MASS jointly delivered by a Consortium of four Universities: Tor Vergata University of Rome, University of Belgrade, University of Bremen, and Universite Côte d'Azur, regulated by the MASS Consortium Agreement and funded by the EU under the call ERASMUS- EDU-2021-PEX-EMJM-MOB.

Contents

Abstract

This thesis investigates azimuthal asymmetries in the dust coma of comet 67P/Churyumov–Gerasimenko using OSIRIS Wide-Angle Camera images from ESA's Rosetta mission. By extracting brightness profiles at projected distances of 10–12 km under near-orthogonal illumination, the study explores how seasonal illumination and nucleus geometry shape the dust distribution in the inner coma.

A Python-based pipeline was developed to automate image selection and azymuthal reflected brightness profile analysis, enabling a consistent treatment of nearly 600 high-quality images. The results confirm the dominance of day-side emission, yet reveal systematic angular offsets between peak brightness and the subsolar direction. These offsets evolve on rotational timescales and vary with sub-spacecraft latitude, showing that viewing geometry and nucleus self-occultation strongly modulate the apparent structure of the coma.

The findings demonstrate that direct insolation alone cannot explain the observed asymmetries; nucleus morphology, heterogeneous surface activity, and thermal response must also be considered. Methodologically, the framework provides a reproducible approach for large-sample image studies, offering empirical constraints for future modeling of coma under different observational and illumination conditions.

Introduction

Comets are believed to be the most pristine remnants of the solar system, bearing witness to the formation of the first planetesimals, building blocks of solid bodies in our system, 4.6 billion years ago (Filacchione et al., 2019; Skorov and Blum, 2012). Formed beyond the snowline in the colder outer regions of the solar system, and although processed by impacts, comets have not undergone significant heating or alteration of their solid materials (de Niem et al., 2018). Unlike asteroids and larger bodies, comets have preserved the imprint of pre-solar materials (Mumma and Charnley, 2011). Therefore, the study of comets offers valuable insights into the formation and early evolution of the solar system.

In addition to their role as time capsules of early solar system material, comets are also key tracers of dynamical and thermal processes. They consist of a mixture of refractory materials, often referred to as dust, and ices. The most abundant volatile species on a typical short-period comet are water (H_2O), carbon dioxide (CO_2) and carbon monoxide (CO) (Le Roy et al., 2015). As they approach the Sun, their volatile ices sublimate, releasing gas and dust, forming a surrounding coma and tail. This process provides a unique opportunity to probe the subsurface composition and structure indirectly (Attree et al., 2024), as well as to study dust–gas interactions that are difficult to reproduce under laboratory conditions. Escort missions like Rosetta have offered an unprecedented opportunity to study small-body activity in real time.

Dust in a comet's coma does not spread uniformly; its spatial distribution at each distance from the nucleus reflects the dynamic interplay between gas drag, solar forces, and surface properties. Figure 1 from (Marschall et al., 2020b) shows the scheme of dust coma structure with dominant forces impacting the trajectory of dust particles with the following description of the regions.

In the near-nucleus region or, so called, coupled coma, (within ∼10 km, or roughly 0–10 comet radii), dust particles are influenced the most by gas drag and gravity exerted by the nucleus. Dust is accelerated by the expanding volatiles flow, producing jet-like filaments that trace back to active surface features such as cliffs and pits (Vincent et al., 2016a; Shi et al., 2018). The coupled coma is optically thin disabling an observer to trace dust structures down to their origins on the surface.

In the transitional coma (10–100 km), dust grains trajectory is being governed not only by the local forces, but also by solar gravity and radiation pressure. In this region dust is completely decoupled from the gas. Larger grains may remain gravitationally bound to the nucleus and can eventually fall back, while smaller, porous particles escape more readily. The size of this region is roughly equal to the Hill radius of the comet, being the extent of gravitational influence of an astronomical body in which it dominates over the gravitational influence of other bodies (Sun in our case).

In the outer coma (beyond ∼100 km or Hill radius), solar gravity and radiation pressure become the dominant forces.

It is necessary to note that this description of coma structure is in reality much more complicated and depends not only on the size and shape of the comet, but also on the dust sizes, the heliocentric distance of the comet, overall activity and its distribution on the surface, etc (Marschall et al., 2020b).

In this research we aim to research the evolution of dust ejecta structures as they transfer from the coupled coma to the transitional coma. Dust ejecta can be classified

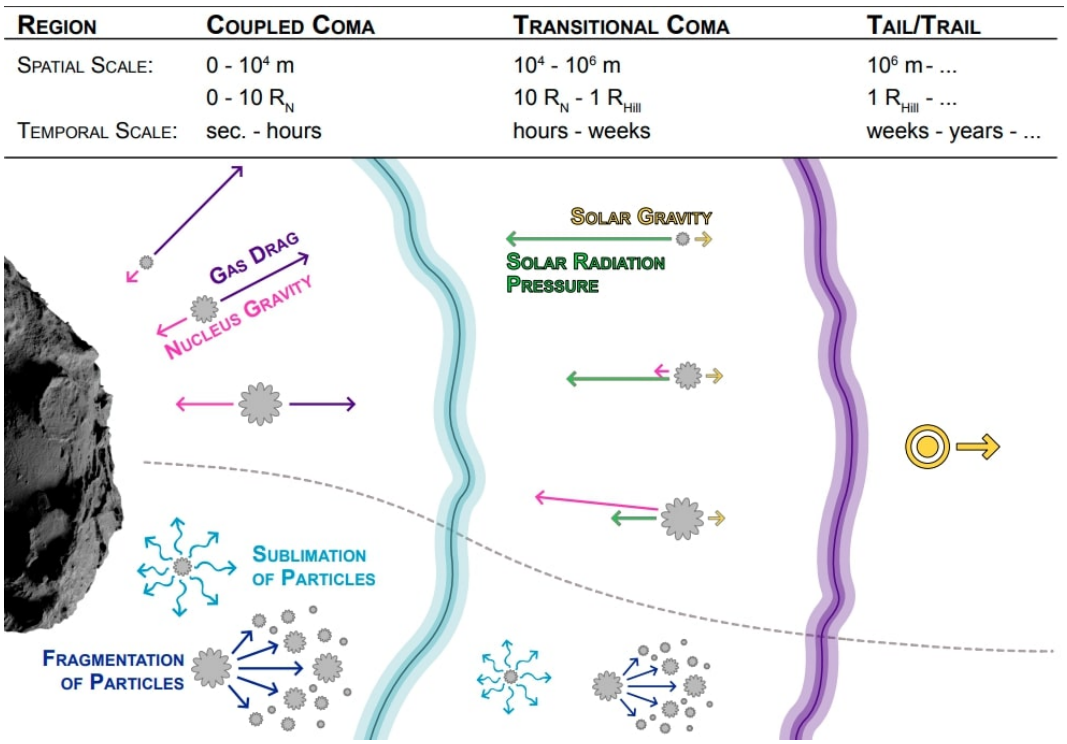

Figure 1: Sketch of the cometary dust environment, divided into three dynamical regions. Region 1: Coupled coma (gas drag and gravity dominate); Region 2: Transitional coma (gas decoupling, solar forces grow); Region 3: Dust tail and trail (solar gravity and radiation pressure dominate). Boundaries vary dynamically and spatially. R_{Hill} is the Hill radius; R_N is the nucleus radius. Adopted from (Marschall et al., 2020b).

into jets and outburst according to their duration and cause.

Outbursts are sudden and short-lived phenomena that can increase the overall brightness of the comet by 2-5 mag. (Hughes, 1975) summarized potential outburst triggering mechanisms, including pressure release from gas trapped in sub-surface pockets, explosive radicals, amorphous-to-crystalline ice transition, impact cratering by boulders, break-up of nucleus, and nuclear crushing. However, this term can be also used for short-lived events less bright than classical outbursts, but a magnitude brighter than usual jets, associated with the release of gas and dust over a duration very short with respect to the rotation period of the nucleus, typically detected in one image only. Such events were attributed to collapse of cliffs or pits exposing fresh volatile-rich material by (Vincent et al., 2016a).

Jets, on the other hand, are relatively steady, collimated streams of dust and gas emitted from specific regions on the comet's surface over hours or days. Jets are driven by solar illumination of active regions. Although jets in a comet's coma often appear as narrow, collimated structures, this appearance can be misleading. As noted by (Sekanina, 1987), any localized active area on a rotating nucleus naturally produces a fan-shaped emission pattern due to the sweeping motion of the source as the nucleus spins. What we observe is a 2D projection of a 3D conical outflow structure, where projection effects enhance the apparent brightness along lines of sight tangential to the cone surface. Therefore, the perceived "jets" are often not truly collimated streams but

geometric illusions created by viewing angle and rotation.

The object of our study is Comet 67P/ Churyumov-Gerasymenko (67P), a short-period comet from the class of Jupiter Family Comet (JFC), discovered by chance on photographic plates on 9 September 1969 by Klim Ivanovich Churyumov (Ukraine SSR) and Svetlana Ivanovna Gerasimenko (Tajikistan SSR).

Comet 67P, as observed by the Rosetta spacecraft, has a peculiar bi-lobed shape with dimensions of 4.3×4.1 km and rotates around a 52°-tilted axis with a rotation period of 12.4 hours (ESA, 2014). This large obliquity leads to strong seasonal effects, with the northern hemisphere experiencing a long, low-activity summer at large heliocentric distances, and the southern hemisphere undergoing a short but intense summer around perihelion. The comet orbits the Sun every 6.43 years, with an aphelion at 5.7 AU and perihelion at 1.2 AU, losing approximately 4.4×10^9 kg of mass during each passage (Pätzold et al., 2019).

As a JFC, the orbit of 67P is currently governed by Jupiter. A particularly close encounter in 1959 (just 0.052 AU from the planet) significantly modified its orbit, reducing its perihelion from 2.74 AU to 1.28 AU and making it a viable target for ESA's Planetary Cornerstone Mission, Rosetta.

Launched on 2 March 2004, Rosetta arrived at comet 67P on 21 November 2014 after a decade-long journey and escorted it for 2.5 years. The mission provided unparalleled spatial, spectral, and temporal coverage of the evolving nucleus and inner coma before, during, and after perihelion (Taylor et al., 2017). Its suite of in-situ and remote sensing instruments captured the dynamics and chemistry of the surrounding dust and gas.

The following is the list of several instruments that were probing coma of 67P:

- **OSIRIS (NAC + WAC):** Captured high-resolution visible images (240-720nm) of the nucleus and coma, enabling analysis of dust brightness, jets, fan structures, and dayside–nightside asymmetries (Keller et al., 2007).
- **VIRTIS-M/H:** An imaging spectrometer that mapped dust and gas emission bands (H_2O, CO_2) from 0.22–5.1 µm, revealing spatial correlations (or lack thereof) between volatiles and dust (Coradini et al., 2007).
- **ROSINA (COPS + DFMS):** Measured neutral gas density and composition with high precision, delivering production rates and surface activity maps (Balsiger et al., 2007).
- **MIRO:** Provided sub-surface temperature profiles and water production rates using sub-mm radiometry (Gulkis et al., 2007).
- **ALICE:** Detected far-UV emissions (e.g., HI Lyman-alpha), complementing gas measurements from ROSINA (Stern et al., 2007).
- **GIADA:** Measured dust momentum and size distributions through direct impacts, contributing to dust-to-gas mass ratio estimates (Colangeli et al., 2007).
- **COSIMA and MIDAS:** Characterized dust grain composition and morphology at micrometer scales (Kissel et al., 2007; Riedler et al., 2007).

A key objective of the Rosetta mission was to investigate cometary activity, specifically the physical mechanisms responsible for the production of dust and gas in the coma (Glassmeier et al., 2007). While the fundamental Whipple model—stating that solar heating causes the sublimation of surface ices, leading to gas outflow that lifts dust (Whipple, 1950)—has been supported by observations of 1P/Halley by Giotto space probe (Whipple, 1986), the finer details of these processes remain debated. Observations have linked dust jets to specific surface regions (Keller et al., 2015; Vincent et al., 2016a), and several models have attempted to describe gas and dust dynamics in the inner coma with varying complexity (e.g., Kramer et al., 2017; Zakharov et al., 2018).

Heterogeneous surface activity, appearing as jets on a comet, does not always signify a heterogeneous nucleus composition; instead, it can arise from a combination of surface processes, topographical effects, and viewing geometry (Marschall et al., 2020a).

Firstly, the irregular shape and complex topography of a cometary nucleus play a significant role. Even with uniform composition, concavities and convexities can focus or de-focus gas and dust flows, creating localized enhancements that appear as collimated jets (Kramer and Noack, 2016; Marschall et al., 2016).

Additionally, dust re-deposition ('airfall') redistributes material: large, slow particles that fail to escape settle into gravitational lows, building smooth mantles that insulate plains while leaving cliffs comparatively baren and thus more active (Vincent et al., 2016b; Marschall et al., 2017).

Secondly, non-uniform solar illumination due to shape, rotation, and self-shadowing produces varied outgassing patterns; projection effects by the observer's viewing angle relative to a rotating nucleus can also make diffuse outflow appear jet-like (Shi et al., 2018).

Seasonality amplifies these patterns on 67P: a short, intense southern summer near perihelion drives strong erosion and a net south to north transport and re-deposition of dust and decimeter-scale 'chunks', with the Hapi neck acting as a key sink that can later reactivate when it re-illuminates (Figure 2 from (Choukroun et al., 2020)). Airfall mantles generally suppress water activity on dusty plains, whereas shadowed Hapi deposits can retain ice and contribute to post-perihelion northern activity; cliffs remain active where fresh material is exposed (Vincent et al., 2016b; Marschall et al., 2017).

There are clear seasonal variations in activity linked to illumination (with water production tracking the subsolar latitude), and many observed changes are evolutionary rather than compositional (Marschall et al., 2020b).

Because seasonal variations in illumination play a significant role in modulating cometary activity it is essential to systematically analyze the dust distribution around the cometary nucleus.

Rosetta's scientific richness also stems from its complex, evolving trajectory, which led to constant variation in observational parameters such as spacecraft–comet distance, phase angle, sub-solar and sub-spacecraft latitudes and longitudes. Figure 3 shows phase angle and cometocentric distance throughout the mission which reflect the complex trajectory of the spacecraft. Such instability of observational conditions made it challenging to repeatedly observe the same region under similar conditions. Consequently, building a consistent and meaningful dataset to study coma evolution, especially in the inner coma, required careful selection. Designing a pipeline to track systemic trends across this irregular dataset was a key aspect of this research.

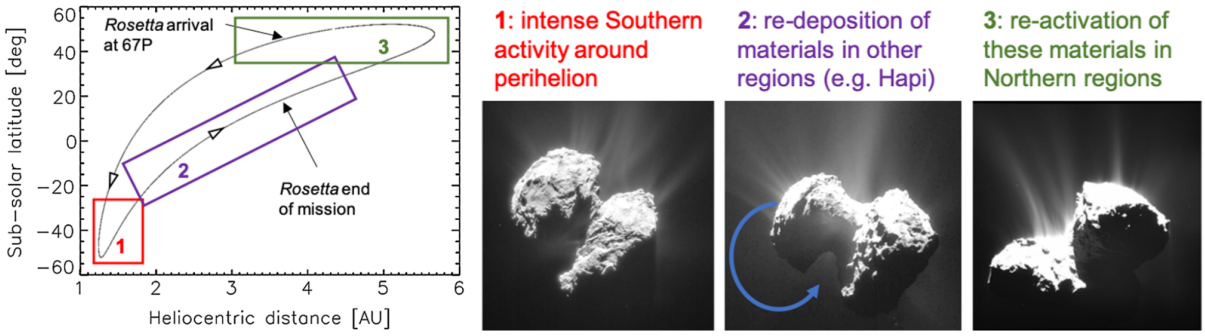

Figure 2: Schematic evolution in activity of 67P along its orbit. **Left:** evolution in sub-solar latitude of a sphere with the same orbital parameters and spin pole orientation as 67P to illustrate the extreme seasonal variability.
Right: Images of 67P's activity at locations along the orbit representative of the three periods mentioned (Credit: ESA/NAVCAM/OSIRIS). Note that the re-deposition of dm-size particles may occur within the perihelion window (1) and up to several months after perihelion ((Bertini et al., 2019)) within period (2). Period (3) consists of the northern summer around aphelion and early during 67P's next approach to the Sun for particles deposited in the Hapi region.
Adopted from (Choukroun et al., 2020).

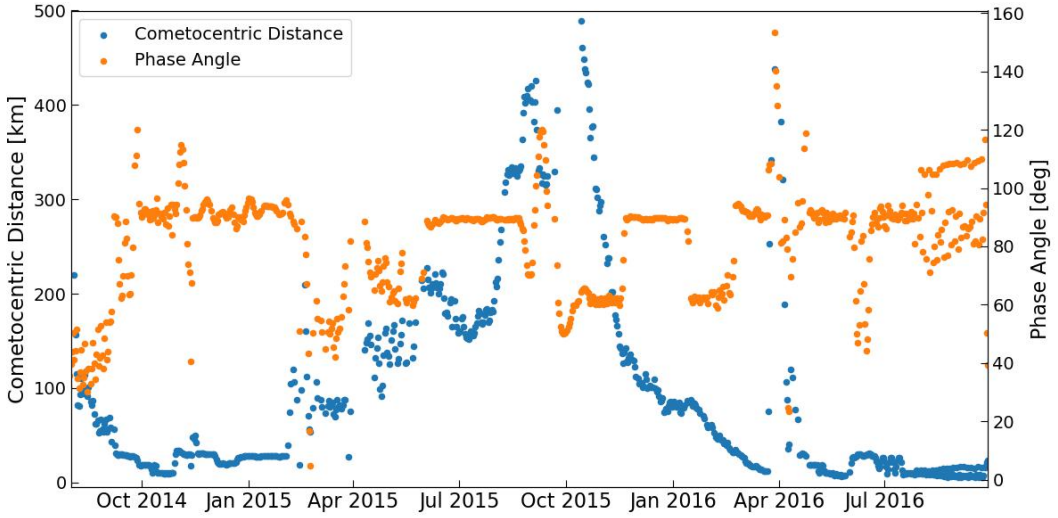

Figure 3: Phase angle (orange) and cometocentric distance (blue), averaged over a day. The plot covers the escort phase from August 2014 to September 2016. Distances ranged from ∼10 km to ∼1000 km, while phase angles varied between 5° and 140°.

The overarching goal of this study is to trace the evolution of dust structures in the inner coma of 67P both before and after perihelion, assessing how seasonal and diurnal variations influence dust production. Similar research on reflected brightness distribution around the comet in an annulus at a fixed radius from the nucleus center (i.e., fixed impact parameter b) has been performed by several authors. These works often link observations to 3D gas-flow modeling (e.g., via Direct Simulation Monte Carlo (DSMC)) to estimate the dust-to-gas production ratio, dust size distributions

(Marschall et al., 2020a), the role of different volatiles (Tubiana et al., 2019), and dayside-to-nightside brightness ratios (Gerig et al., 2021).

Because DSMC simulations are computationally expensive, most prior studies focused on short time intervals with a limited number of images (e.g., (Tubiana et al., 2019) used 15 images from 27 April 2015). In contrast, our goal is to select a broader, high-quality dataset suited for modeling or empirical analysis of dust structures throughout the full escort phase.

During my internship, I developed a Python-based pipeline to efficiently select and analyze approximately 30,000 images acquired by Rosetta's Optical, Spectroscopic, and Infrared Remote Imaging System (OSIRIS) cameras. This framework enables the measurement of brightness distributions with any OSIRIS filter, at different distances from nucleus center, and for any mission phase satisfying geometric and quality constraints. This allows us to study how seasonal and diurnal cycles govern dust emission and coma morphology.

1 Dataset and Geometric Selection

1.1 Preliminary Dataset

In our research we used data from Rosetta's OSIRIS Wide Angle Camera (WAC) found on Planetary Science Archive (PSA), in which data from Rosetta instruments are arranged into datasets. Each dataset contains all data files belonging to a single camera (e.g., OSINAC or OSIWAC), mission period, and data product (Deller, 2020). Data product refers here to a standardized version of the set of images at a specific processing level, packaged with metadata, meant for a particular kind of scientific use (e.g., raw, radiometrically calibrated, georeferenced). Figure 4 shows the number of images taken by each camera, grouped by five keyword tags. Out of roughly 70,000 images, we focused primarily on coma images—most of which contain the keyword "dust"—but selected them using a custom pipeline rather than simple keyword searches.

This subsection is dedicated to the description of our dataset choices and the selection pipeline.

1.1.1 OSIRIS WAC

OSIRIS was the scientific camera system on board Rosetta. It comprises a Narrow Angle Camera (NAC) and a WAC with a field of view (FOV) of about $2.20° \times 2.22°$ ($18.6\,\mu$rad/pxl) and $11.35° \times 12.11°$ ($101.0\,\mu$rad/pxl), respectively. Both cameras use a 16 bit 2048×2048 pixel backside illuminated CCD detector with a UV-optimized anti-reflection coating (Keller et al., 2007).

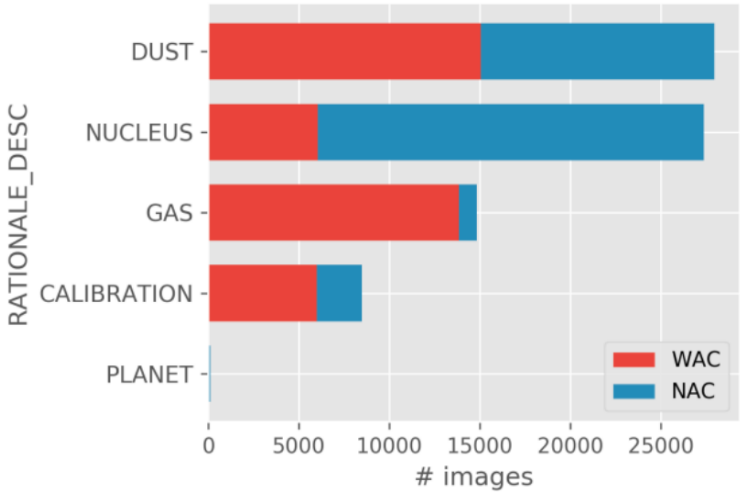

Figure 4: Number of images per keyword, that was assigned to all images taken after hibernation exit on 2014-01-17 (Deller, 2020)

The NAC is equipped with 11 filters covering a wavelength range from 250 nm to 1000 nm, while the WAC has 14 filters covering a range from 240 nm to 720 nm (see transmission curves Figure 5).

The NAC and WAC have been designed as a complementary pair:

- NAC, with its high spatial resolution, was used to detect the nucleus of 67P/Churyumov-Gerasimenko from a distance of millions of kilometers and then to study the morphology of the surface and details of the dust ejection process.
- WAC The WAC has lower spatial resolution but a much wider field of view, allowing it to observe gas and dust flow even when the spacecraft is close to the nucleus. This provides valuable context for other instruments.

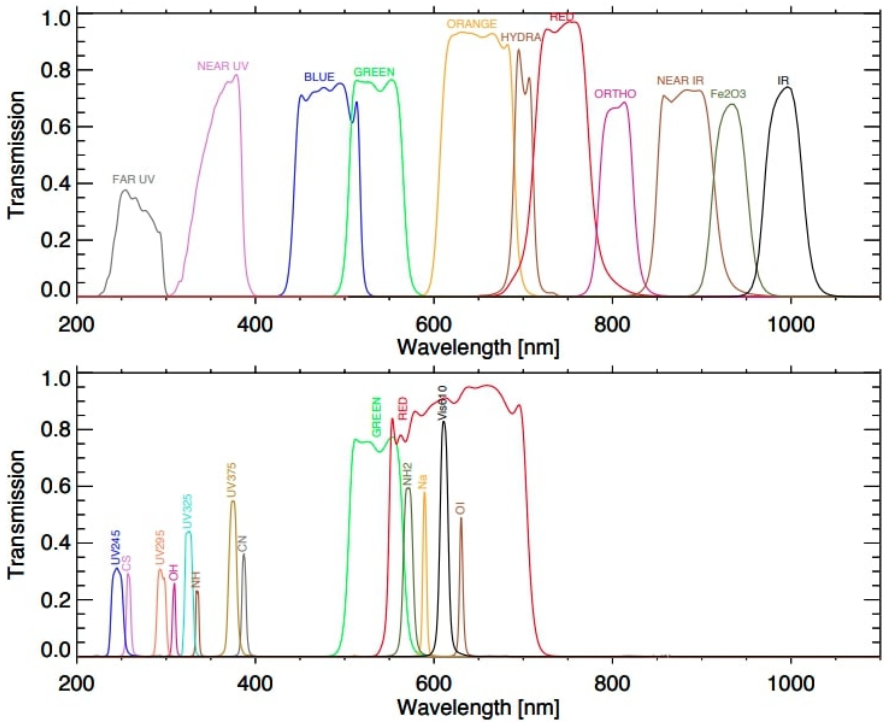

Figure 5: Comparison of transmission curves of OSIRIS Narrow-angle camera (*top panel*) and Wide-angle camera (*bottom panel*) filters ((Tubiana et al., 2015)).

Because we are more interested in the dust ejecta, we chose WAC data for the preliminary analysis because we expect more images with a field of view including the whole nucleus.

Among the WAC filters there are two broad-band filters (Red and Green), the rest are narrow-band filters, some of which are tuned to strong emission lines of the most abundant gas species in the coma (CS, OH, NH, CN, NH_2, Na, OI).

For this study, we worked with the Vis-610 filter (F18) with $\lambda_0 = 612.6\,\mathrm{nm}$ and width $\Delta\lambda = 9.8\,\mathrm{nm}$. Alternatively, NAC Orange (F22) filter could be used as it is a standard reference filter with $\lambda_0 = 649.2\,\mathrm{nm}$ and width $\Delta\lambda = 84.5\,\mathrm{nm}$, corresponding to wide visible filter ((Oklay, 2015)).

The Vis-610 filter was selected as the primary one for several reasons: a) it has been used in multiple previous studies on dust distribution in the coma, making our results easier to compare with existing literature (Gerig et al., 2021; Tubiana et al., 2019); b) other narrow-band filters are tuned to gas emission lines, which would potentially contaminate our dataset with gas contributions.

1.1.2 Data processing level

The OSIRIS data are provided in various data products, from raw data to georeferenced data. We were using CODMAC level 4 (OSIRIS level 3F) that represents image data files (PDS3 IMG or FITs files) transformed from radiometric units $[Wm^{-2}sr^{-1}nm^{-1}]$ into dimensionless reflectance units with calibrated header and corrections for solar stray-light, in-field stray-light, radiometric & geometric distortion, and boresight ((Deller, 2020)). This is the highest level of calibration currently available on the PSA.

1.1.3 Mission planning interval selection

The seasonal illumination cycle of comet 67P, driven by its extreme axial tilt of approximately 52°, leads to significant variations in dust activity and coma structure throughout its 6.45-year orbit. The obliquity of the rotational axis causes the subsolar latitude to oscillate between $+52°$ and $-52°$ (Figure 6), resulting in highly asymmetric and temporally uneven heating patterns across the surface. For nearly four years near aphelion (at ~ 5.68 AU), the northern hemisphere experiences cool summer, while the southern hemisphere experiences extended darkness (e.g., Anhur region (Filacchione et al., 2019)). As the comet approaches perihelion (1.24 AU), the subsolar point rapidly migrates southward, producing a short but intense southern summer (see Figure 6). This season is characterized by elevated insolation, strong outgassing, and peak dust production. The heating pattern asymmetry results in the majority of cometary activity occurring around-perihelion, concentrated in the southern hemisphere.

Solar illumination patterns on 67P is conceptually similar to Earth's seasonal cycle, where the axial tilt governs the latitudinal migration of the subsolar point. However, due to 67P's much higher obliquity and eccentricity, the resulting seasonal contrasts in insolation are far more extreme, producing sharp asymmetries in surface heating and volatile activity. These variations play a central role in modulating the spatial and temporal structure of the dust coma.

To systematically investigate how these seasonal variations influence the brightness distribution—particularly at fixed phase angles—we selected mission intervals that correspond to distinct illumination states.

Rosetta's operations were organized into 35 Mid-Term Planning cycles (hereafter, MTPs), each spanning approximately four weeks. Each MTP was subdivided into Short-Term Planning cycles (STPs), typically lasting one week. The comet escort phase extended from November 2014 (MTP10) to the end of the mission in September 2016 (MTP35), providing a rich dataset that spans a broad range of heliocentric distances and seasonal configurations. Figure 6 illustrates the evolution of the subsolar latitude as a function of heliocentric distance and serves as a guide for identifying MTPs suitable for capturing different seasonal conditions in the coma.

1.2 Selecting for Viewing Geometry

MTPs 10 to 35, with appropriate data levels, collectively contain over 30,000 images, ranging from close-up views of the comet to wider contextual perspectives where dust structures are more visible.

After selecting the instrument, data processing level, and observational time frame,

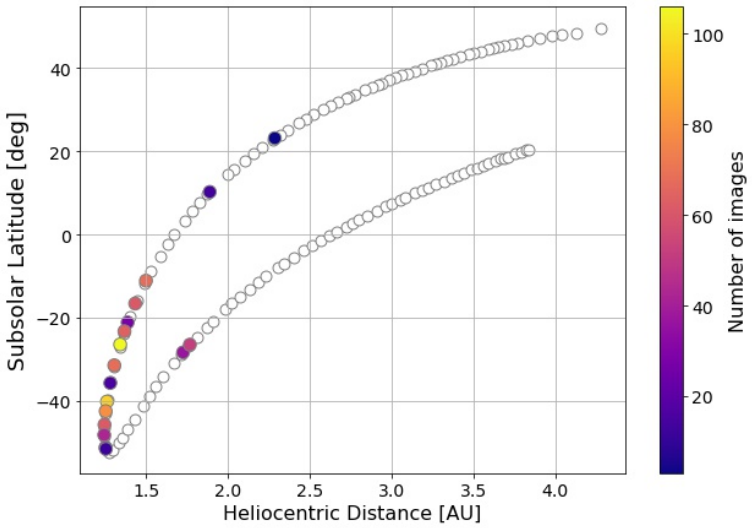

Figure 6: Subsolar latitude and heliocentric distance of 67P averaged by STPs ($\sim$ week- long mission planning units) and color-coded for number of images in each STP. The median of 73 STPs (MTP10-35) is 34 images per STP.

the next step was to identify and implement the selection criteria for observational geometry which yeilded consistance to a very diverse dataset.

Given the impracticality of manually selecting useful images, it was necessary to establish objective criteria for image selection. To address this, I utilized a database (Marschall, private communication) which contained file names from the older PSA system along with key observational parameters such as field of view and nucleus center pixels, which are often missing in the IMG files headers.

1.2.1 Phase Angle

The first selection criteria was for an observation to have a phase angle $85^\circ < \phi < 95^\circ$. The phase angle is an angle between the line of sight of the spacecraft and the Sun to object vector. It is preferred to select images taken at phase angle close to 90° due to several reasons.

Firstly, at a 90-degree phase angle, the observer is looking directly at the terminator (the line separating the illuminated dayside from the shaded nightside). This geometry allows for a clear distinction between the coma above the sunlit hemisphere and the coma above the shadowed hemisphere.

Secondly, this criterium allows us to simplify viewing geometry to 2D image fixing Sun strictly under the sub solar point on the comet. When the phase angle deviates significantly from 90 degrees, projection effects can distort the observed dayside-to-nightside (DS:NS) brightness ratio. Observing from directly above the terminator minimizes these effects, ensuring that the measured brightness accurately reflects the dust distribution above each hemisphere.

Unfortunately, as was shown in Figure 3, the phase angle wasn't fixed during Rosetta mission and only a small number of images are made at precisely straight phase angle.Therefor, we chose the range of values above.

1.2.2 Impact Parameter

To ensure consistent measurements across varying spacecraft distances, we defined a fixed projected distance, known as the impact parameter, from the nucleus center at which to analyze the coma brightness. Since images were taken at various stages of Rosetta's orbit, selecting an appropriate impact parameter helps standardize our sampling ring across the dataset. Additionally, the impact parameter must fall entirely within the image frame, which constrains our minimum field-of-view and usable image subset.

The choice of impact parameter is closely tied to the physical regimes of dust dynamics in the coma. At smaller distances, the dust is still strongly influenced by gas drag and nucleus gravity, leading to lateral transport and complex flow patterns. At larger distances, however, the dust enters a free-radial outflow regime where particles move roughly radially from the nucleus at near-constant velocity (Zakharov et al., 2018; Gerig et al., 2018). Under this approximation, the reflected brightness becomes proportional to the projected column density and is expected to follow a '1/r' falloff.

To evaluate when this assumption becomes valid, we refer to the concept of the average azimuthal dust reflectance introduced by Gerig et al. (2018). Instead of analysing brightness along individual radial cuts, this method integrates the dust reflectance along a full circular path at a given impact parameter, effectively averaging over all azimuthal angles. The result is a radial profile of the mean coma brightness that is less sensitive to local jets or geometric projection effects. When multiplied by the impact parameter, $\bar{A}$-curve (see Figure 7) should remain constant if the dust follows free-radial outflow with a '1/r' dependence. Deviations from constancy close to the nucleus reveal additional processes such as dust acceleration, lateral transport, sublimation, fragmentation, or the influence of the nucleus' finite size.

(Gerig et al., 2018) demonstrated that beyond $\sim 11.9 \pm 2.8\,\mathrm{km}$ (or roughly six average cometary radii) the azimuthal reflectance profiles show reduced angular variation (Figure 7 (right))and follow a nearly constant $b \cdot A(\theta)$ trend, where $A(\theta)$ is the average reflectance and b the impact parameter. This behavior is consistent with the expected $1/r$ decline in column density and serves as an observational threshold for the onset of steady outflow.

For this study we established a limit of $b \geq 10$ km, lower than suggested by (Gerig et al., 2018). This decision was made to balance data availability and validity of free-flow assumption, as the upper limit on impact parameter and therefore field of view is set by the observational constraints of Rosetta's orbit: the bigger b, the less available images of the comet we have.

As the whole nucleus and impact distance should be within the frame, we imposed a condition on the X- and Y- axis:

$$b_{pxl} < (X,\, Y)_c < (X,\, Y)_{max} - b_{pxl} \tag{1}$$

$$b_{pxl} = \frac{2b}{D\,\theta} \tag{2}$$

In Equation 2 b_{pxl} is the impact parameter in pixels, $(X,\, Y)_{max}$ is the dimension of an image, and $(X,\, Y)_c$ are the coordinates of nucleus' center. The impact parameter b_{pxl} [pxl] is calculated individually for every image as Equation 1, where b is the impact

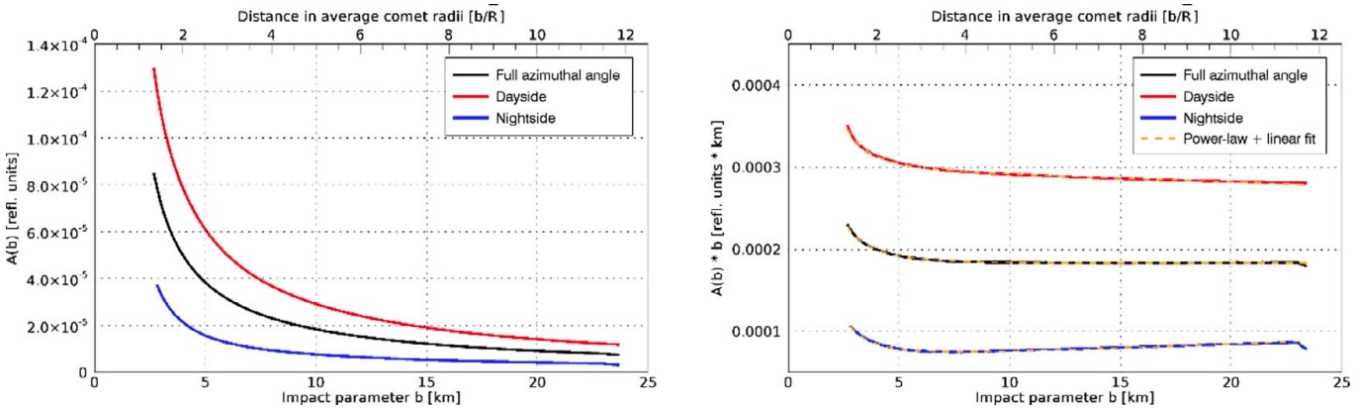

Figure 7: **Left:** Average azimuthal dust reflectance profiles at increasing impact parameters, extracted from OSIRIS WAC images. Each curve represents the mean reflectance measured along a circular ring centered on the nucleus, as a function of azimuthal angle. Curves are shown for the full 360°, the sunward hemisphere (dayside, 180°–360°), and the anti-sunward hemisphere (nightside, 0°–180°).
Right: Same reflectance profiles multiplied by the impact parameter b, illustrating the deviation from the expected '1/r' dependence in the inner coma. The flattening of the $b \cdot A$ curve at larger distances indicates that the dust distribution approaches free-radial outflow behavior beyond $b \sim 11.9$ km. Adapted from (Gerig et al., 2018)

parameter in [km], $D\,[km]$ is the cometocentric distance at the time of the exposure, and $\theta = 101.0\,\mu$rad/pxl is the angular resolution.

The results of the selection procedure can be seen in Figure 6. Colored markers indicate STPs that meet the criteria, with the color intensity reflecting the number of available images per STP. Selected MTPs (colored points on Figure 6 and listed in Table 1) conveniently fall into different seasons: pre-perihelion, close pre-perihelion, and post-perihelion.

1.3 Quality Control

The conventional way to assess the quality of data is to obtain signal to noise ratio (SNR) for the image. In our case, the signal is the intensity or radiance measured on a circle of radius $b = 10$ from the cometary nucleus and the noise will be the intensity of background measured far from the nucleus (Figure 8). The SNR for each image was calculated by first dividing the intensity of each pixel along the sampling circle by the average background intensity (blue rectangle in Figure 8), and then averaging these individual pixel SNR values across the entire circle.

However, having high SNR doesn't necessarily mean that the image will be suitable for intensity distribution analysis due to inhomogenuity of the signal, because SNR is averaged across 360 bins. Therefore, we decided to use total variation TV defined in Equation 3 and relative total variation TV_{rel} defined in Equation 4 to asses images.

$$TV = \sum_{i=1}^{N} |I_i - I_{i+1}| \tag{3}$$

Figure 8: OSIRIS WAC image of the cometary nucleus. For SNR signal is measured on the circle of 10 km radius (red line) and compared to background noise averaged on a 400 x 400 pxl square (in blue). Orange dotted line is the radius of integration $b + db$ where $db = 0.5\,km$ Image: W20150623T091403778ID4FF18.IMG

$$TV_{rel} = \frac{1}{360} \sum_{i=1}^{N} \frac{|I_i - I_{i+1}|}{I_i} \tag{4}$$

Total variation is the difference between each intensity (I_i) and its neighbor (I_{i+1}) summed over all intensities. As we visualize the intensity distribution in a polar histogram over 1° bins, total variation will be difference between column height of adjacent bins (the green lines in Figure 9). The relative total variation is the normalized sum of differences between adjacent bins, divided by their respective intensities, and averaged over 360°to quantify the percentage of variation across the intensity distribution of a single image. This metric allows us to account for the shape and smoothness of the distribution independently of its absolute intensity values. A high relative total variation indicates a spiky distribution with rapid changes between adjacent angular bins (left example in Figure 9), which could be the result of cosmic rays or CCD corruption and uncalibrated image artefacts. A low relative total variation suggests a smoother and more continuous profile (right example on Figure 9), which is generally more suitable for identifying dominant emission directions and estimating angular offsets.

In Figure 9 are the two images with their respective intensity distributions. Right one has a much smaller total variation, is smoother, doesn't have negative intensity values, and overall is easier to interpret.

To increase SNR, smoothen the intensity distributions, and make more images elegible for the analysis intensity was integrated in range $[b, b+db]$ where $b = 10\,km$ and $db = 0.5\,km$ (Figure 8). Figure 10 shows comparison of relative total variaton and SNR for images with intensity measured on a circle (left), and intensity integrated radially (right). The signal was amplified drasticly, and the difference between the adjacent

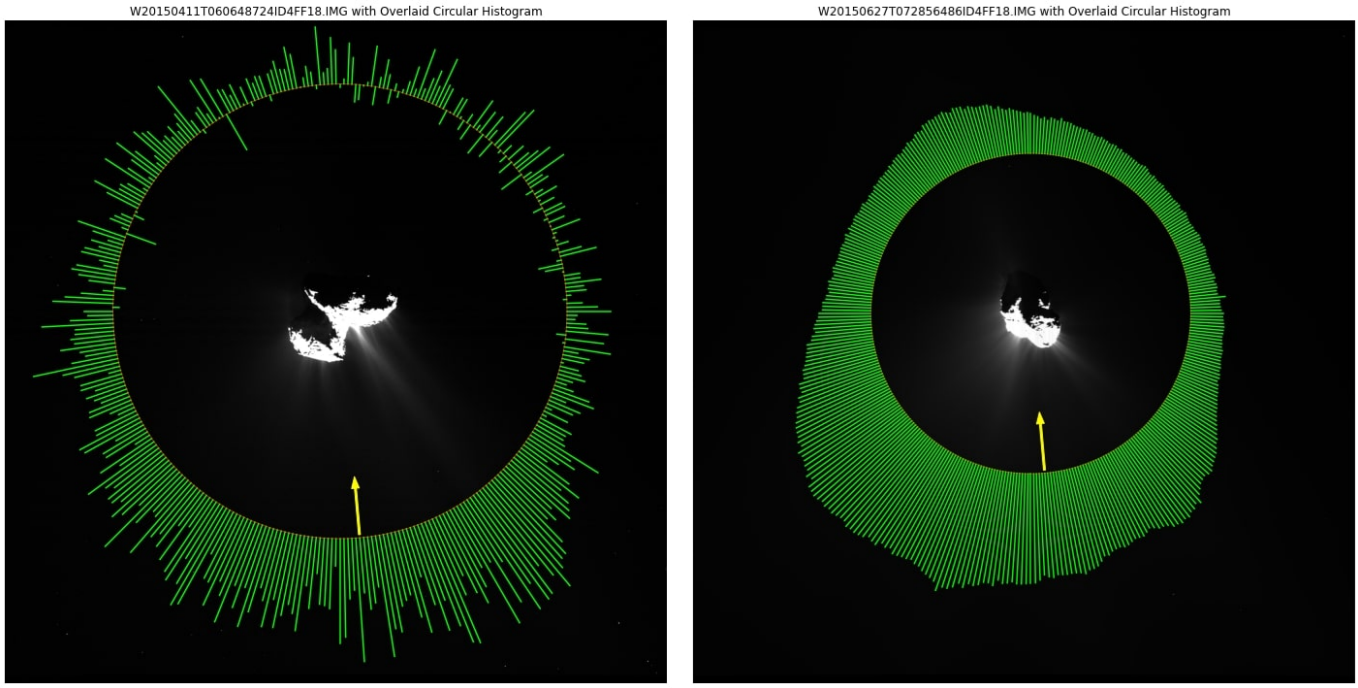

Figure 9: Comparison of spiky and smooth intensity distributions and their signal to noise ratio, total variation, and relative total variation.
Left: $SNR_0 = 1.9$, $TV_0 = 51$, $TV_{rel0} = 833$. After integration between b and db values improved a lot: $SNR_{int} = 32$, $TV_{int} = 51$, $TV_{rel_{int}} = 265$.
Right: $SNR_0 = 8$, $TV_0 = 4.4$, $TV_{rel0} = 9.9$. After integration between b and db: $SNR_{int} = 95$, $TV_{int} = 4.4$, $TV_{rel_{int}} = 6.6$.

histogram bins became less, which is reflected in less disperse distribution of the relative total variations of images (scale of change can also be seen in values for individual images Figure 9).

Using the method above we had to discard only 30% of our selected subset and retain 596 images out of 851 selected initially by the criteria of subsection 1.2.

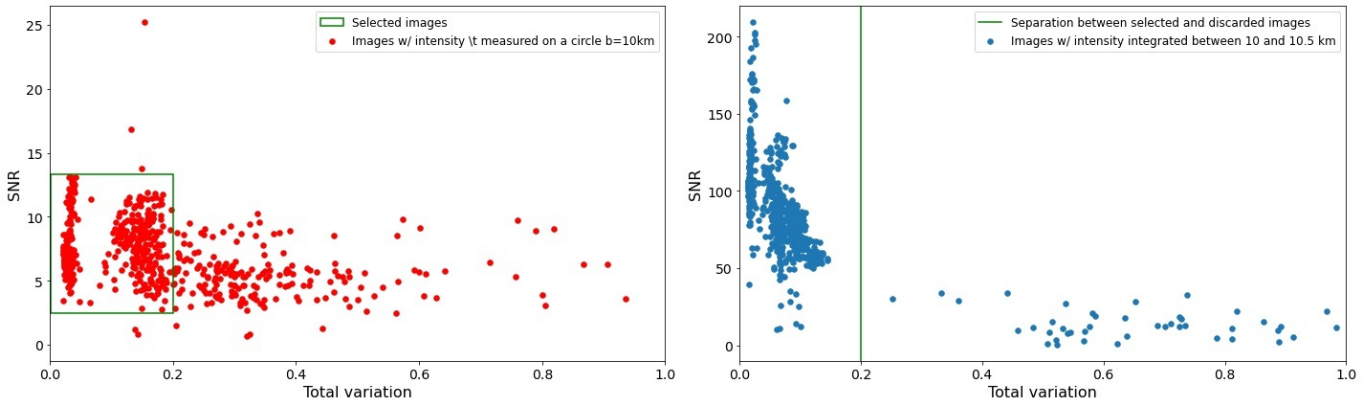

Figure 10: Signal-to-noise ratio against relative total variation (in units of initial subset).
Left: Images were selected in the range $TV_{rel} = [0, 0.2]$ and $SNR = [2.5, 12.5]$. This corresponds to 45% of the previous subset.
Right: Images were selected in the range $TV_{rel} = [0, 0.2]$, corresponding to 70% of the previous subset.

Table 1: Overview of dataset of OSIRIS WAC images selected according to criteria listed in subsection 1.2 before excluding images with low SNR and high relative total variation.

MTP	STP	Heliocentric distance, AU	Subsolar latitude, deg	Number of images
013	044	2.29 to 2.25	23.19 to 23.16	3
015	051	1.89 to 1.86	10.31 to 10.19	14
017	059,60,61,62	1.51 to 1.35	-10.54 to -24.40	221
018	063,64,65,66	1.35 to 1.26	-25.54 to -40.72	287
019	067,68,69,70	1.26 to 1.24	to 1.25 and -42.07 to -51.26	224
020	071	1.25 to 1.26	-51.55 to -51.56	12
023	083,84	1.69 to 1.77	-28.60 to -26.36	89

2 Brightness Profile Analysis

2.1 DS:NS Ratio

In order to test the robustness and performance of our selection and analysis procedures, we decided to replicate the results presented in (Gerig et al., 2021) concerning dayside-to-nightside ratio.

The dayside-to-nightside (DS:NS) brightness ratio is useful for our research, because it allows us to assess the spatial asymmetry of dust activity around comet 67P and evolution of seasonal activity. DS:NS ratio quantifies how much brighter the illuminated (dayside) hemisphere of the coma is compared to the shadowed (nightside) hemisphere, offering a proxy for how effectively solar insolation drives dust production. (Gerig et al., 2021) used this ratio to track seasonal and heliocentric variations in dust emission, revealing significant contribution of nightside to the total brightness on the sample circle. Numerical simulations employed in their research confirm that direct activity on the nightside contributes to $\sim 10\%$ of total emission.

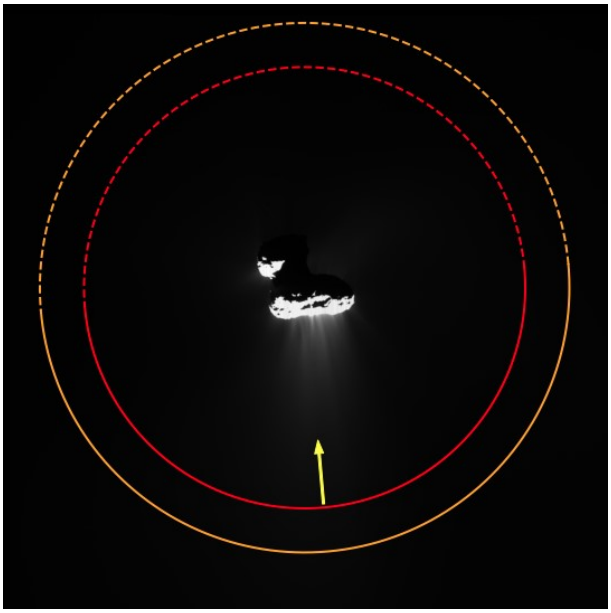

Figure 11: Demonstration of dayside (in solid line) and nightside (in dashed line) parts of the azymuthal profile, where the brightness measured and compared to calculate DS:NS ratio. Inner (red) circle has radius of impact parameter $b = 10\,\mathrm{km}$, outer (orange) circle has radius of 12 km and is the outer limit of brightness integration. W20150701T193811499ID4FF18.IMG

To calculate DS:NS we employ the same idea of azymuthal average profile ($\overline{A(\theta)\,b}$) as explained in subsection 1.2 defined in terms of azimuthal angle θ in Equation 5 with $A(\theta, b)$ the image brightness as a function of azimuthal angle and impact parameter.

$$\overline{A\,b} = \frac{b}{2\pi}\int_0^{2\pi} A(\theta, b)d\theta \tag{5}$$

For the dayside brightness $(\overline{A\,b})_{\mathrm{DS}}$, the integration in Equation 5 is performed over the angular range $\theta \in \left[-\frac{\pi}{2}, \frac{\pi}{2}\right]$, where the subsolar direction is at $\theta = 0$. Analogously,

the nightside brightness $(\overline{A\,b})_{\mathrm{NS}}$ is computed over $\theta \in \left[\frac{\pi}{2}, \frac{3\pi}{2}\right]$. This angular partition allows the dayside-to-nightside (DS:NS) brightness ratio to be calculated as:

$$\mathrm{DS:NS} = \frac{\int_{r_1}^{r_2} (\overline{A\,b})_{\mathrm{DS}}\, db}{\int_{r_1}^{r_2} (\overline{A\,b})_{\mathrm{NS}}\, db} \tag{6}$$

Same as in the original study we used limits of integration $r_1 = 10\,\mathrm{km}$ and $r_2 = 12\,\mathrm{km}$.

Figure 12 shows the comparison of our plot (bottom panel) of DS:NS seasonal evolution to the one from the original paper. While the main trend and its magnitude are preserved in our plot, we have more data points (16 STPs or weeks were used instead of 12, as in original data) which change the average value and scale of the plot.

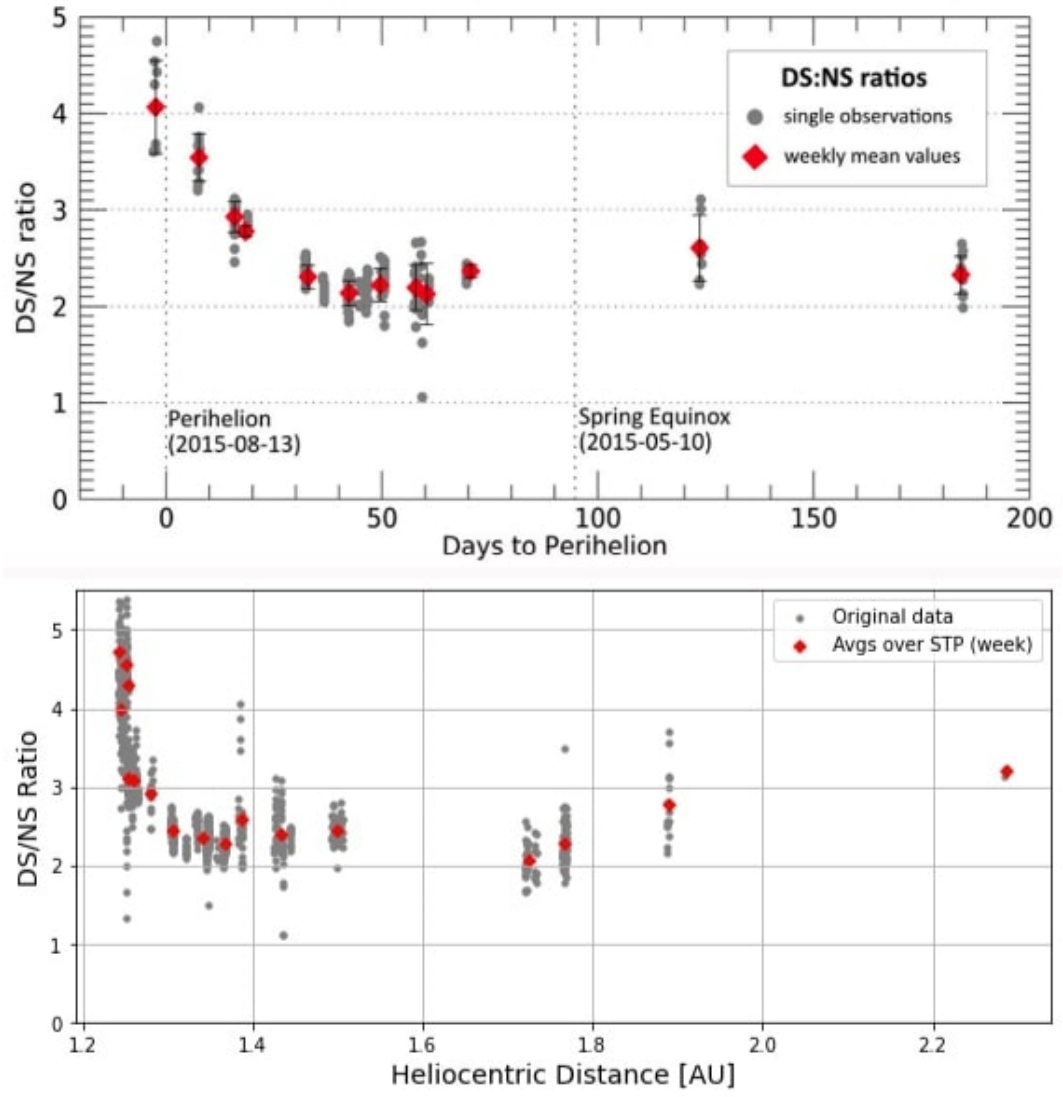

Figure 12: Dayside to nightside ratio seasonal evolution. Gray points are measurements averaged over a day and red diamonds are weekly averages.
Top panel:DS:NS ratio against days to perihelion from (Gerig et al., 2021).
Bottom panel: DS:NS tratio agains heliocentric distance produced by our pipeline.

(Gerig et al., 2021) also suggested that the increase in dayside activity and therefore the increased brightness of the dayside coma does not result in the same increase in the observed nightside brightness. To investigate this claim, we examined the evolution of total brightness for the dayside and nightside separately as a function of heliocentric distance.

Figure 13 shows the measured brightness on the dayside (red) and nightside (blue) for all selected images, as well as the average values binned by The Rosetta Short-Term Planning-cycle (STP), marked in yellow. The plot shows a systematic difference: while the dayside brightness shows significant variability and a general increase near perihelion ($\sim$ 1.24 AU), the nightside brightness remains consistently lower and exhibits a much flatter trend. This supports the hypothesis that even during periods of elevated solar insolation and outgassing, the enhancement of activity is primarily confined to the illuminated hemisphere. The limited response on the nightside suggests that thermal lag or other delayed heating mechanisms do not significantly contribute to dust brightness at the distances sampled.

Another interesting detail in Figure 13 (right) is the peak of both night- and dayside brightnesses comes a month prior to perehelion. This fact is worth investigating more closely by expanding dataset to include later dates in September to include solstice and compare the trend of dayside brightness to dust production rates over the same time interval.

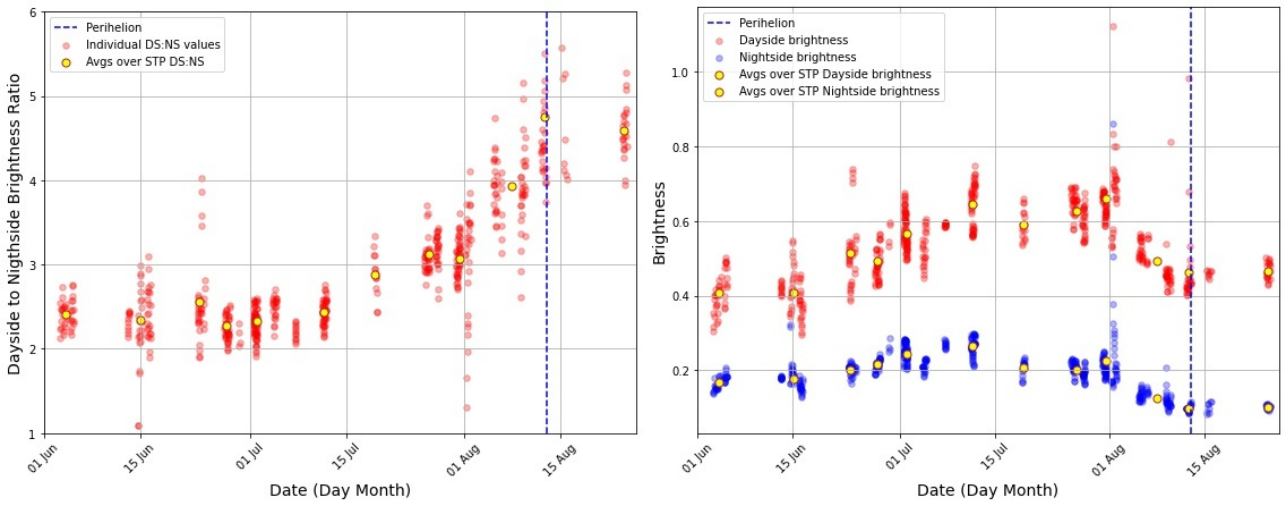

Figure 13: **Left:** Dayside to nightside brightness ratio over time. Yellow points are the averages over STP (a week).
Right: Dayside brightness (red) and nightside brightness (blue) seasonal evolution with yellow points being weekly averages.

2.2 Peak offset

While the DS:NS brightness ratio offers a valuable large-scale diagnostic of hemispheric asymmetry, it does not capture directional structure in the dust outflow. To investigate these azimuthal asymmetries in more detail, we examined whether the brightest jet in the coma, the azimuthal peak of the intensity distribution, systematically aligns with

the subsolar point. In a purely illumination-driven outflow scenario with a spherical nucleus, one would expect the brightness maximum to coincide with the subsolar direction, and the minimum to lie directly opposite. However, our results reveal consistent angular offsets from this idealized geometry.

Before showing and explaining these results, let's visualize the peak offset. Figure 14 shows the azymuthal profile split in 4 unequal sectors, with 0° being the subsolar direction. During the selection described in subsection 1.2, we discarded observations with phase angle outside $\theta \in [85°, 95°]$, so we can safely assume the Sun and therefore the illumination peak being right bellow the comet and coinciding with the subsolar direction.

This way if the main peak of intensity distribution has negative peak offset (like on the Figure 14), it is shifted in the direction of the dawn. Conversely, a shift to the right, or in the positive direction means that peak being moving towards the dusk side.

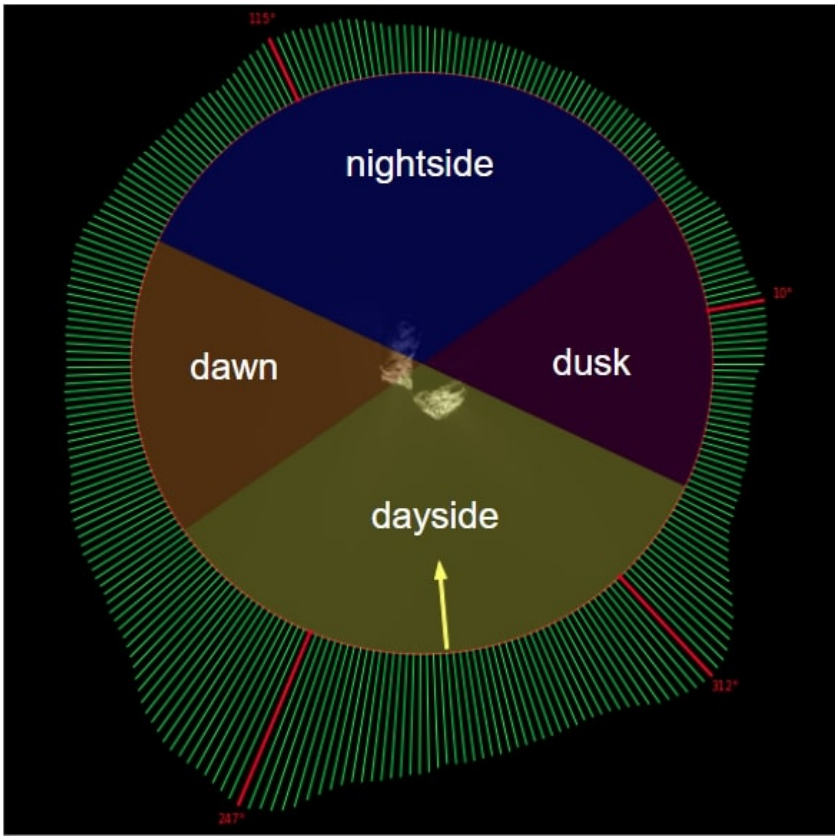

Figure 14: Nucleus of 67P with overlapping diagram of azymuthal sectors. Yellow arrow indicates subsolar direction taken as 0°. Azymuthal profile is separated in the following sectors: Dayside($-60° < \psi < +60°$), dusk ($+60° < \psi < +120°$), nightside ($+120° < \psi < +240°$), and dawn ($+240° < \psi < +300°$).

Integrating intensity along the radius for every bin as explained in subsection 1.3 allows to determine angular location of the primary peak of the intensity distribution pretty reliably in all of the selected dataset and calculate peak offset from the fixed subsolar direction.

Figure 15 shows the seasonal changes in the highest peak of intensity distribution with time. It is clear from the figure that the peak rarely coincides with the subsolar

direction. Colors indicate different subsolar latitude corresponding to change of seasons.

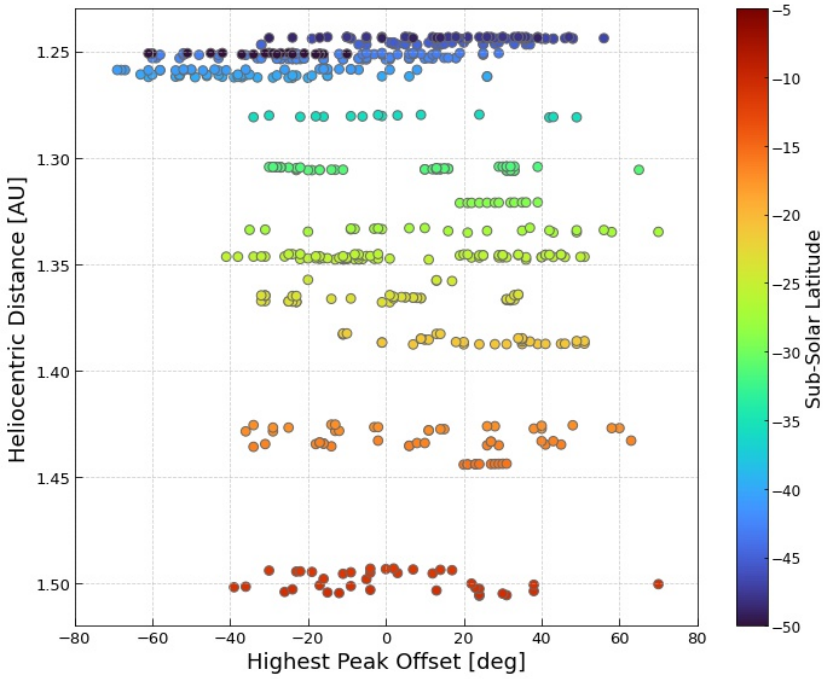

Figure 15: Peak offset angle from subsolar direction (taken at 0°) and its seasonal evolution.

Some STPs seem to have more negative offset (post-perihelium MTP023P), while other have a wider offset to the positive side. Statistical analysis of peak offset distribution in different MTPs didn't give any correlations between peak offset and other characteristics like subsolar latitude, DS:NS, etc. However, we noticed that on diagrams of peak offset evolving with subsolar longitude (proxy for local time on the comet), images of the same day or several days follow specific patterns (Figure 16 left).

Even though, there are hundreds of data points, orange-red parallel diagonal lines and green vertical lines stand out. These lines not only have similar sub-spacecraft latitude, but also correspond to the same observation date. Figure 16 (right) shows the two sets of observations: 27.06.205 (blue) with peak offset skipping from negative to positive offset without a smooth transition and 01 & 04.07.2015 (orange and yellow), where we see diagonal lines moving across the 0° line with time.

Because 67P's rotation period is $\sim 12\,h$, we see two cometary rotations in the plots for each observation date. These trends are conserved during both periods, meaning that they are not caused by some temporary phenomenon. Moreover, these trends are true for other dates across different STPs (Figure 35). Due to mirroring by OSIRIS WAC camera, in our data comet rotates from left to right (from dawn to dusk as Figure 14). In the current dataset east longitude was chosen, meaning that sub-solar longitude decreases with time.

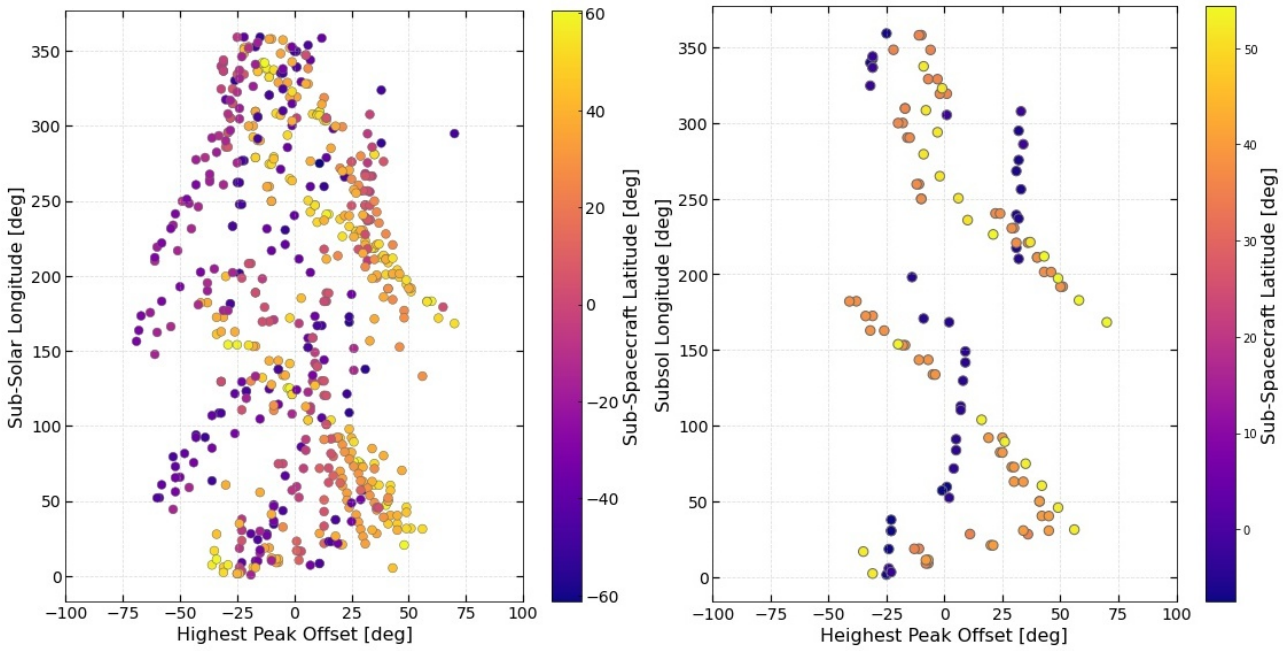

Figure 16: Highest peak offset against sub-solar longitude color-coded for values of sub-spacecraft latitude
Left: For the whole dataset;
Right: For 27.06.2015 (blue, with sub-spacecraft latitude in narrow range $[-7°, -2°]$) and 01 and 04.07.2015(yellow and orange with sub-spacecraft latitude in wider range $[35°, 51°]$).

3 Interpretation and Physical context

In this chapter we will be describing and explaining the peak offset vs subsolar longitude diagram, image by image to follow the trend and attempt to connect the intensity peaks to the probable surface regions of origin. Simulation of the nucleus activity was not in the scope of this project, so we cannot confidently connect the peaks to a specific location on the nucleus. That is why we will use very generalized names for the parts of 67P. We call the larger lobe of 67P - 'body' and the smaller lobe - 'head', they are connected by an active region commonly called 'neck'. On Figure 17 the neck is colored in yellow, flat part of the body (opposite side to the junction of lobes) is colored in red and will be referred to as 'foot' and the part of the smaller lobe opposite to the neck will be referred to as 'head'.

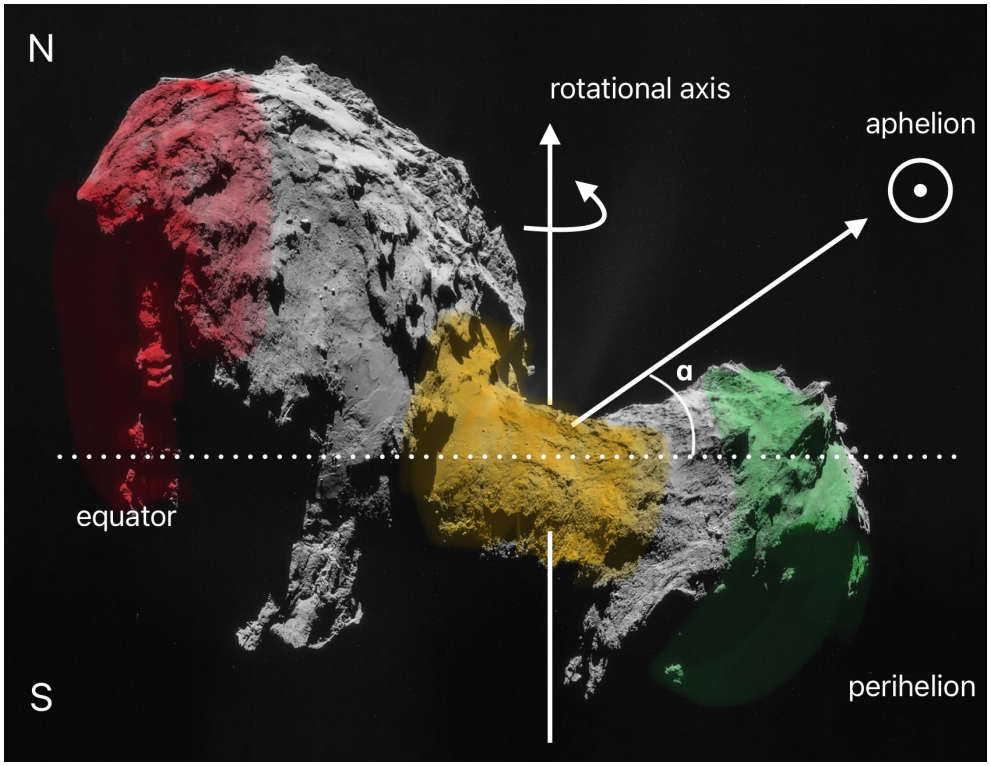

Figure 17: Generalized segmentation of comet 67P used for interpreting peak brightness directions. The neck (yellow) connects the smaller 'head' lobe (green) and the larger 'body' lobe. The red area marks the flat region on the body's far side, referred to as the 'foot'. The equator and rotational axis are shown schematically. The arrow points toward the Sun and α angle is subsolar latitude defining seasons. OSIRIS WAC image of the comet.

In sections subsection 3.1 and subsection 3.2 we will be describing the behavior of the azymuthal brightness profile for the two cases (Figure 18) separately and show 8 images marking the transitional moments of the patterns for each case.

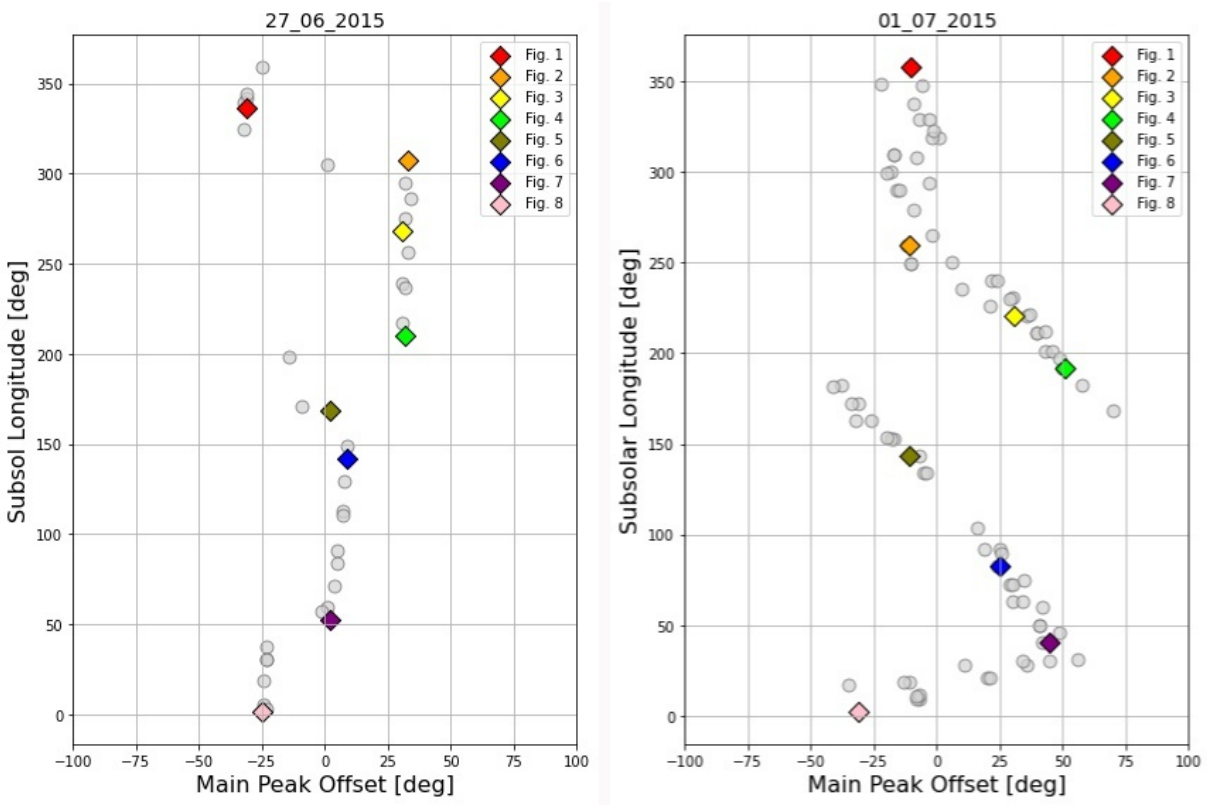

Figure 18: Offset of the main intensity distribution peak from subsolar direction at 0° as a function of subsolar longitude.
27.06.2015 (left) Peak skips from very negative ($< -25°$ offset between 360° and 300° of subsolar longitude)to very positive values ($> +25°$ offset between 300° and 200°), then it stays close to subsolar direction ($\sim 0°$ offset between 200° and 50°)and skips to negative side again (~ -25 offset between 50° and 0°);
01,04.07.2015 (right) Between 360° and 300° subsolar longitude, peak oscillates in range of $[-25°, +5°]$ offset. Next from 300° to 200°, peak smoothly moves further into positive values up to +50° offset. Approximately between 200° and 150° subsolar longitude peak skips between drastically positive and negative offset values. After that up until $\sim 50°$ longitude peak smoothly moves from $-10°$ to +50. Last portion between 50° and 0° longitude peak transitions swiftly from +50° to $< -25°$ offset.

3.1 27.06.2015

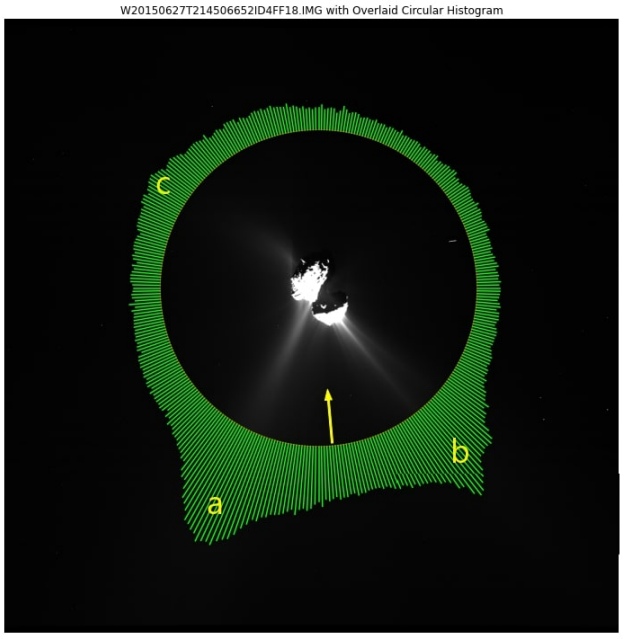

Figure 19: Subsolar Longitude: 336° W20150627T214506652ID4FF18.IMG corresponding to Fig. 1 on Figure 18 (left).

At the initial moment, we see two peaks: one on the dawn side (peak (a) with negative offset from subsolar direction), opposite to the neck, and one on the dusk side (peak (b) with positive offset), opposite to the head. There is also a decreasing peak on the border of the dawn and nightside, opposite to the foot (c). The strongest peak (a) has a gaussian form, while the secondary peak has a more complicated structure.

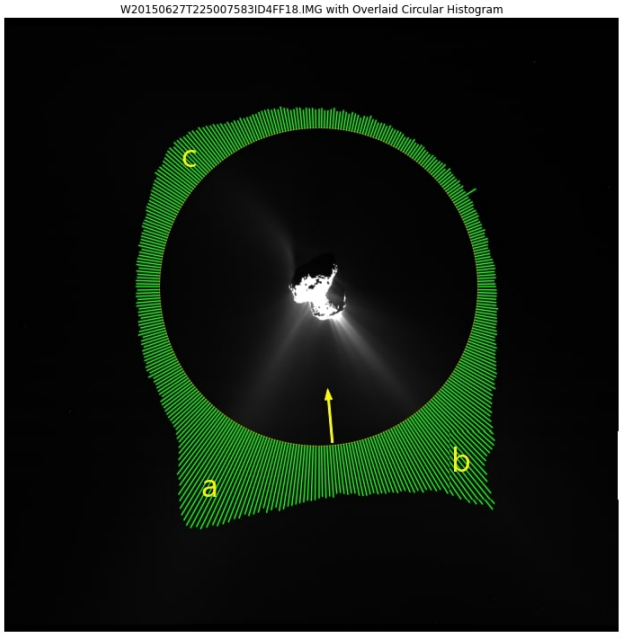

Figure 20: Subsolar Longitude: 305° W20150627T225007583ID4FF18.IMG corresponding to Fig. 2 on Figure 18 (left).

Around 295° subsolar longitude, the peak (b) on the dusk side overpowers the dawn peak (a) (leading to a sudden skip from negative to positive peak offset angle), and the peak (c) opposite to the foot becomes more pronounced. Intensity peak (b) may represent combination of jets originating in the neck in head in the line of sight of spacecraft.

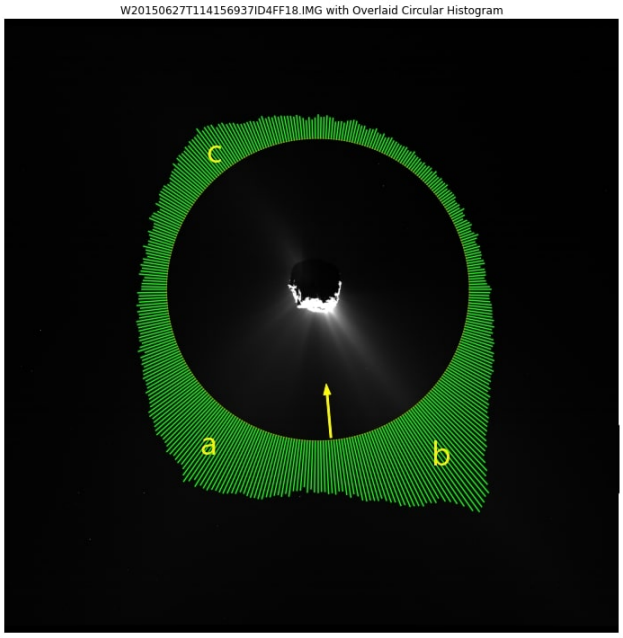

Figure 21: Subsolar Longitude: 268° W20150627T114156937ID4FF18.IMG corresponding to Fig 3. on Figure 18 (left).

The dominating peak (b) on the dusk side becomes broader as head disappears behind the body and we see mainly the foot of the comet in our line of sight. Peak (a)on the dawns side also broadens, while peak (c) remains constant in shape and position. The azymuthal distribution suggests that the major peak is connected to the neck region, because the head can no longer contribute to the peak. The jet from the head would probably point in the opposite direction to the camera due to 67P's shape.

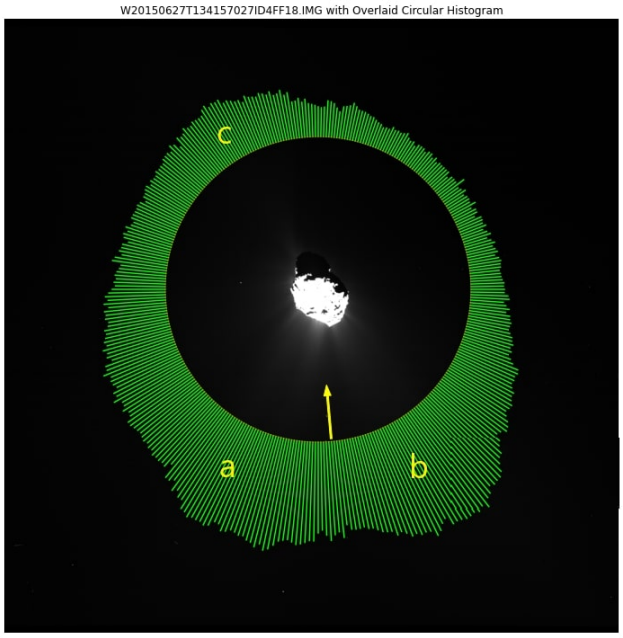

Figure 22: Subsolar Longitude: 210° W20150627T134157027ID4FF18.IMG corresponding to Fig 4. on Figure 18 (left).

As the head slowly emerges from the opposite side, we still observe two similar peaks on the dawn (a) and dusk (b) sides, with the dusk side still being stronger. A peak on the nightside is also visible. Peaks (a) and (b) move closer to subsolar direction as the foot gets progressively more illumination and starts to contribute to the detected intensity distribution.

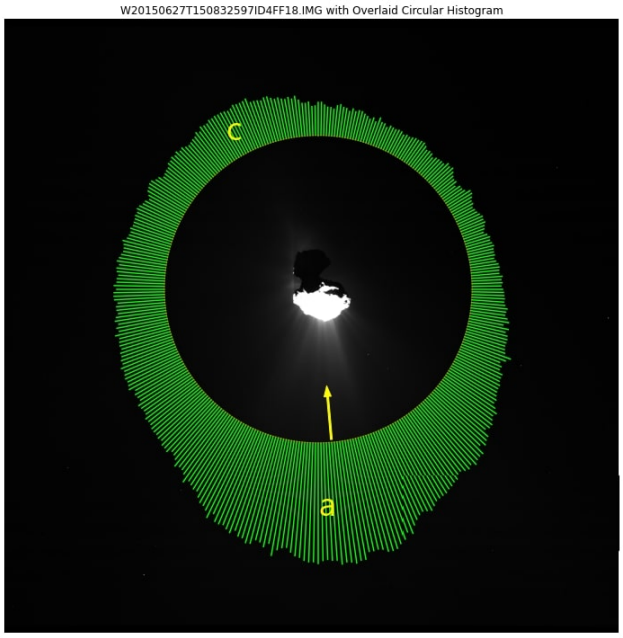

Figure 23: Subsolar Longitude: 168° W20150627T150832597ID4FF18.IMG corresponding to Fig. 5 on Figure 18 (left).

Between 210° and 198°, the peak shifts from positive to negative, and the two peak merge into one broad peak (a) around the subsolar direction, as the comet's foot becomes illuminated. During the interval $[210°, 140°]$ subsolar longitude, we don't see a distinctive contribution of neck region, however there is asymmetry in the profiles on the dawn and dusk sides, with brightness detected on the dusk side being higher.

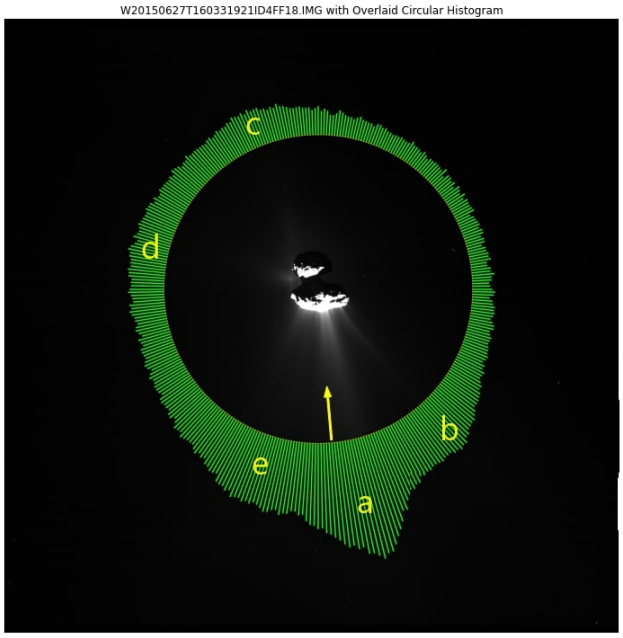

Figure 24: Subsolar Longitude: 141° W20150627T160331921ID4FF18.IMG corresponding to Fig. 6 on Figure 18 (left).

From 168° to 140°, the central peak now splits into three peaks (a) - the strongest, narrow peak shifting toward the dusk side (resulting in positive main peak offset), (b) and (e) on the opposite sides of peak (a). On the overexposed OSIRIS WASC image we can see the three distinct jets coming from across the foot.
From 141° to 70°, the shape remains almost constant, with a slightly growing peak on the nightside and asymmetric dawn side peak (d) forming opposite to the neck.

Figure 25: Subsolar Longitude: 60° W20150627T062847804ID4FF18.IMG corresponding to Fig. 7 on Figure 18 (left).

Around 60° subsolar longitude, the head is aligned with the line of sight of the spacecraft, and the subsolar-direction peak becomes broader again and more irregular due to activity from the illuminated neck region. Peaks (d) and (e)from Figure 24 are following the neck and eventually merge into peak (d). The main peak (a) remains near the subsolar direction, while a secondary peak (c) on the negative side grows stronger.

Figure 26: Subsolar Longitude: 1.5° W20150627T082847935ID4FF18.IMG corresponding to Fig. 8 on Figure 18 (left).

Between 52° and 37°, the peak (a) broadens and shifts further to the negative side, opposite to the neck. A second peak opposite to the head (b) also becomes more distinct as both peaks sharpen. Having neck and head illuminated results in multiple peaks across the distribution. We can attribute peak (c) to the neck activity and peaks (e) and (d) to combinations of neck and foot activity.

3.2 01.07.2015

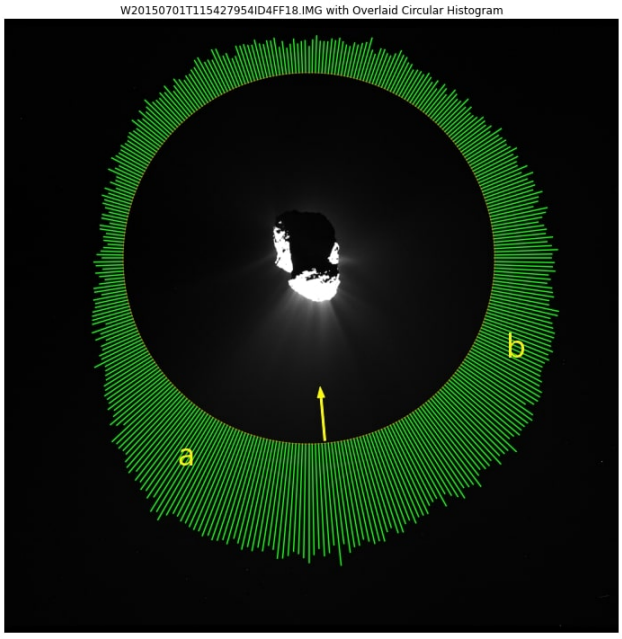

Figure 27: Subsolar Longitude: 337° W20150701T115427954ID4FF18.IMG corresponding to Fig. 1 on Figure 18 (right).

At the initial moment we see the head in front of the body, head and neck being illuminated. Intensity distribution is broad and pretty uniform with intensity with rounded peak (a) at dawn side (resulting in the negative peak offset angle) with an asymmetrical intensity enhancement on the dusk side (b). This broad distribution is probably connected to both neck and head.

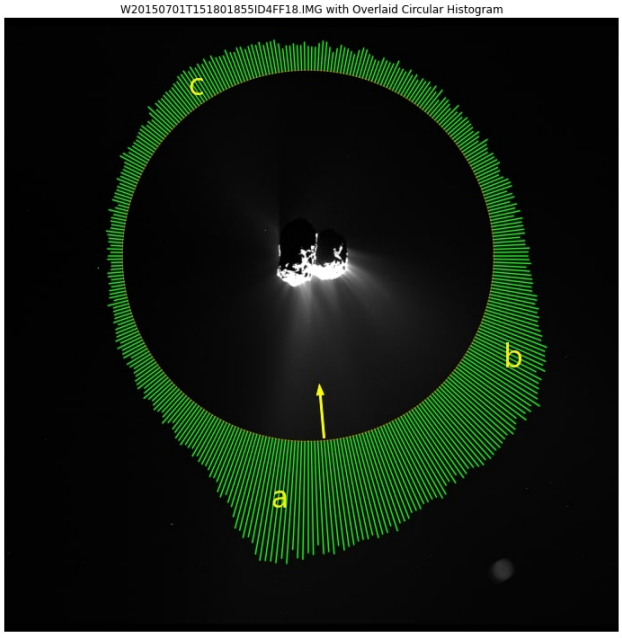

Figure 28: Subsolar Longitude: 259° W20150701T151801855ID4FF18.IMG corresponding to Fig. 2 on Figure 18 (right).

The trend is conserved until approximately 300° subsolar longitude, when peak (a) narrows and gets more pronounced on the dawn side opposite to the neck. Another crest looking peak (b) appears on the dusk side following the head. Drastic decrease in intensity in the dawn side left from the peak (a) is probably caused by the shape of the body lobe that leads to shading the foot from illumination.
After 250° subsolar longitude, activity from the neck is focused in the direction of rotation towards dusk and the highest peak (a) starts moving to more positive offset values.

Figure 29: Subsolar Longitude: 220° W20150701T163811492ID4FF18.IMG corresponding to Fig. 3 on Figure 18 (right).

Both neck and head produce a single merged broad peak (a). Around 225° subsolar longitude, when the foot gets illuminated, the peak opposite to it (b) starts to grow. Main peak (a) is still moving with the neck toward more positive values in the dawn side.

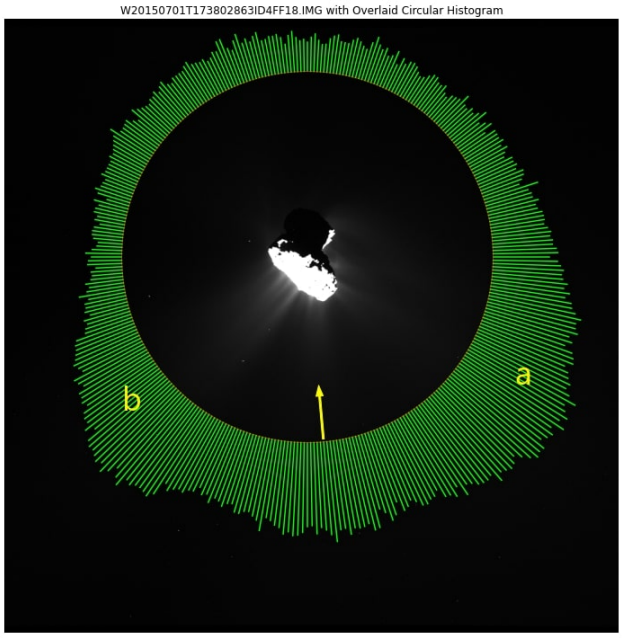

Figure 30: Subsolar Longitude: 191° W20150701T173802863ID4FF18.IMG corresponding to Fig. 4 on Figure 18 (right).

Secondary peak (b) opposite to the foot grows as the foot gets more illuminated. At 191° subsolar longitude main peak opposite to the neck is driven to its maximum position on the dusk side (+50°). At 182° secondary peak (b) opposite to the foot overpowers (a) and becomes the main intensity peak on the dawn side (resulting in maximum negative offset of −41°).

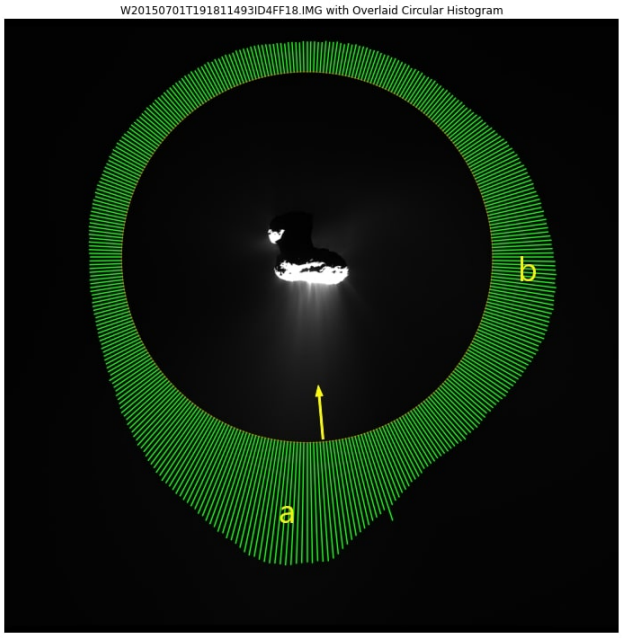

Figure 31: Subsolar Longitude: 143° W20150701T191811493ID4FF18.IMG corresponding to Fig. 5 on Figure 18 (right).

There are two distinct peaks: main peak opposite to the foot (now called (a)) and secondary peak (b) opposite to the neck following the rotation. Peak offset is smoothly moving from negative to positive offset values, while peak (b) wanes, due to the neck being cut off from illumination and shaded by the foot.

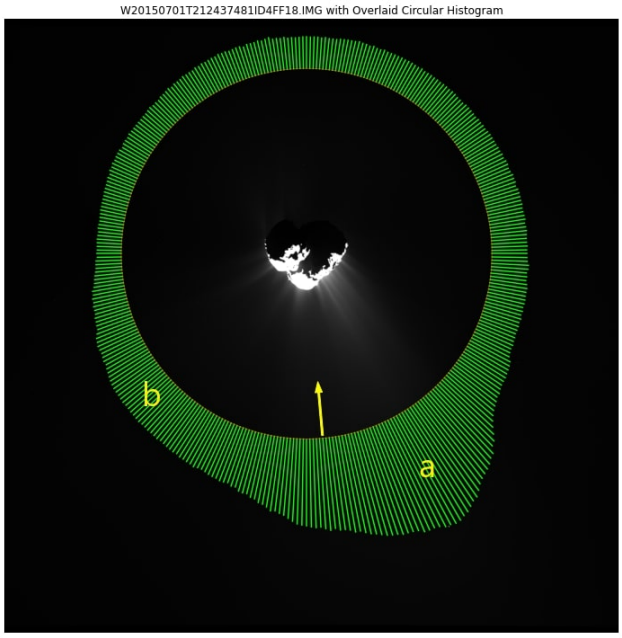

Figure 32: Subsolar Longitude: 82° W20150701T212437481ID4FF18.IMG corresponding to Fig. 6 on Figure 18 (right).

There is a gap in data between 133° and 92° subsolar longitude. But it is safe to assume that the main and only peak (a) opposite to the foot is passing subsolar direction towards dusk side (resulting in positive offset angle). As neck starts to get more sunlight, the peak (b) opposite to it starts to form, while the main peak is moving further to dusk.

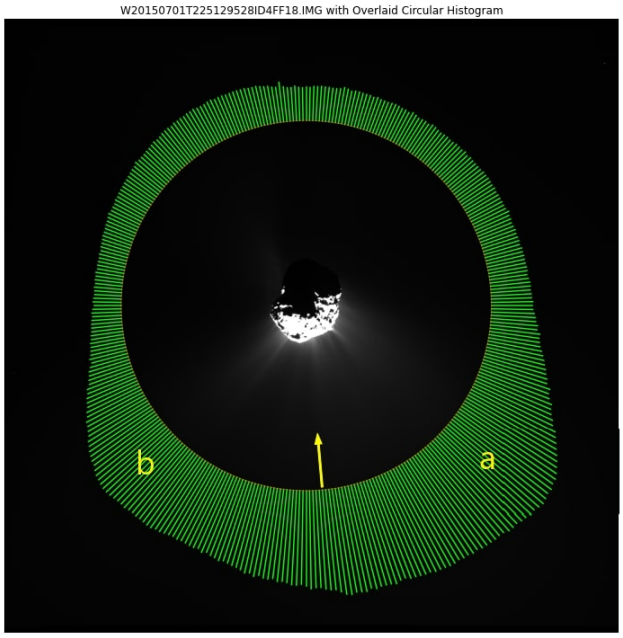

Figure 33: Subsolar Longitude: 40° W20150701T225129528ID4FF18.IMG corresponding to Fig. 7 on Figure 18 (right).

As the head is aligned with the camera we see a broad crest of distribution with two peaks on both dusk (a) and dawn (b) associated with combination of head and neck activity.

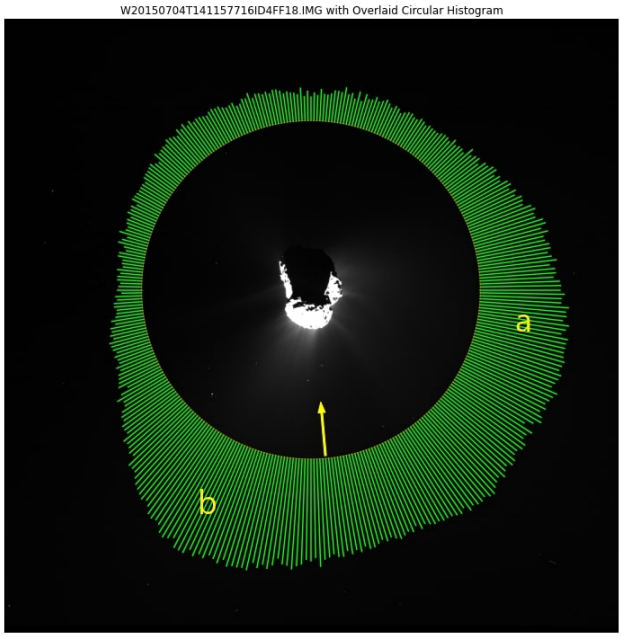

Figure 34: Subsolar Longitude: 2° W20150704T141157716ID4FF18.IMG corresponding to Fig. 8 on Figure 18 (right).

Even though the trend continues until the end of the period, peak (b) on the dawn side starts dominating the one on dusk (a) around 20° subsolar longitude, as the peak on the dusk side moves further from subsolar direction. The dominating peak of the broad distribution on dawn side (b) may be caused by combination of jets from neck and head results in a negative offset.

3.3 Interpretation of peak offset pattern

27.06.2015 and 01.07.2015 are two of few dates that have such an extensive coverage of comet's rotation with nearly static observational conditions: phase angle close to 90° and subspacecraft latitude changing in a very narrow range.

The common thing about these two cases is the regions activity is coming from (neck, head, foot) and the tendency of intensity peaks to follow the activity region for a short while after there is no more direct illumination. During the two periods peak offset takes both negative and positive values with no particular preference. However, the transition of the peak happens in a very different way in these two cases: one has constant peak location and then jumps across the diagram, and the other transitions smoothly from negative to positive values.

We conclude that this discrepancy stems directly from the geometry of observations. This doesn't exclude the effect of different surface composition of activity centers and thermal lag on shaping dust distribution. The angle between the rotation axis and spacecraft's line of sight (defined as sub-spacecraft latitude) is playing a major role in shaping the intensity distribution and its diurnal evolution. On Figure 16 (right) you can see that the two datasets lie in different ranges of sub-spacecraft latitude: 27.06.2015 in [2°, 6°] and 01 & 04.07.2015 in [35°, 51°]. This is also confirmed by the other observation dates with similar sub-spacecraft latitudes.

Figure 35 (left) shows our 01.07.2015 dataset and 3 other days. Described above in subsection 3.2, peak offset moves from negative to positive values and is marked by yellow dots. It is worth noting that in other days (26,28 & 31) peak offset retains the form but mirrors the evolution pattern: instead of moving from left to right, it transitions from right to left. These patterns and their corresponding sub-spacecraft latitudes are a good indication of observational geometry impact on the peak offset.

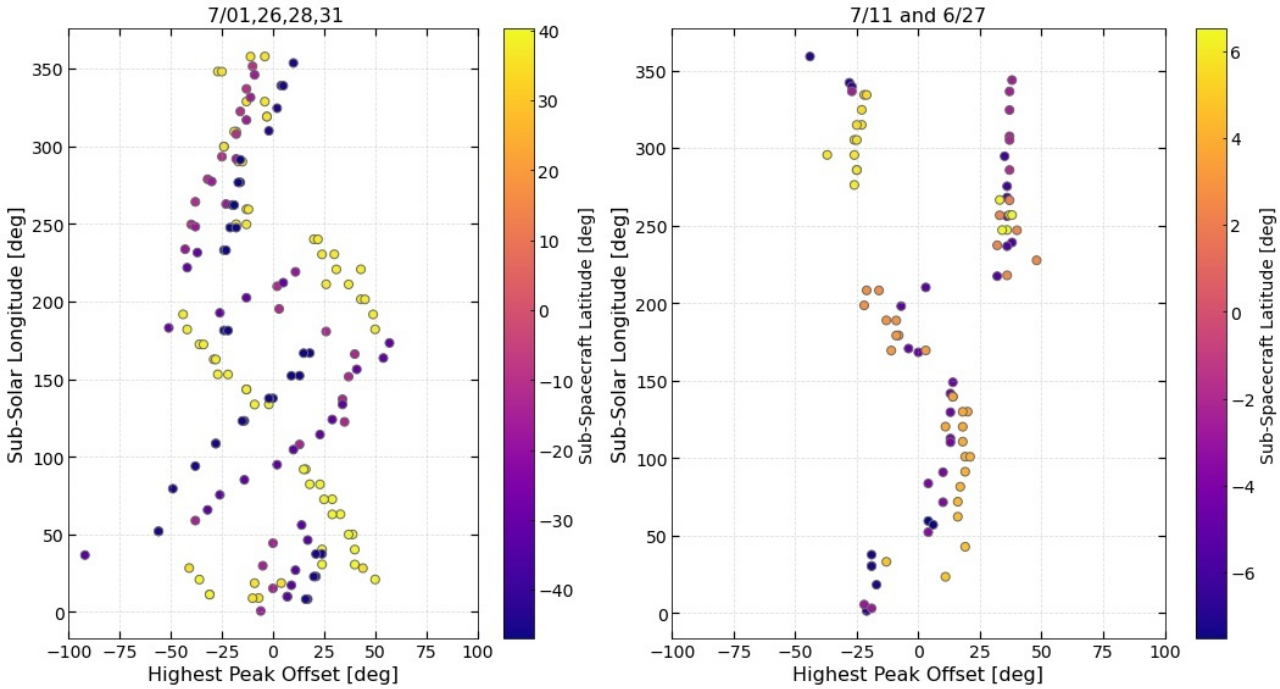

Figure 35: Highest peak offset against sub-solar longitude color-coded for values of sub-spacecraft latitude

Left: 3 days in July (26,28,31) in comparison to July 1st. 26,28, and 31.07 have a wide range negative sub-spacecraft latitudes and produce pattern of peak offset mirroring the 1st July pattern described in subsection 3.2.

Right: Comparison of July 11th to June 27th described in subsection 3.1.

Conclusion

This thesis set out to quantify and interpret azimuthal asymmetries in the inner dust coma of comet 67P/Churyumov–Gerasimenko, using OSIRIS/WAC Vis-610 images under near-orthogonal illumination and a fixed projected sampling distance. By combining a strict geometric selection ($\phi \sim 90°$; $b = 10 - 12\,km$) with a reproducible Python pipeline for azimuthal profile extraction and quality control, we built a consistent dataset across different observational conditions and used it to probe how illumination, viewing geometry, and complex bilobal shape of the cometary nucleus influence the coma's brightness distribution.

Methodologically, the work contributes a practical framework for large-sample image studies of the inner coma. Key choices included (i) selecting WAC/Vis-610 to minimize gas-line contamination, (ii) enforcing phase-angle and field-of-view constraints so that the subsolar direction is well defined in image space, and (iii) applying signal-aware quality metrics (SNR together with total variation (TV, TV_{rel})) and radial integration (10–10.5 km) to enhance signal while preserving directional information. After quality control, 596 of 851 geometrically eligible images remained.

Three main scientific results emerge. First, the dayside–to–nightside (DS:NS) brightness ratio reproduces the known seasonal trend and amplitude while extending the temporal sampling (more STPs) relative to prior work (Gerig et al., 2021). The dayside brightness increases strongly as 67P approaches perihelion, whereas the nightside brightness experiences weak and more smooth increase, indicating that enhanced insolation primarily amplifies activity on the illuminated hemisphere with only a limited, delayed, or geometrically suppressed response on the nightside at the sampled distances. This result reinforces the view that direct insolation dominates dust release at this scale, with only a modest contribution from nightside sources or thermal-lag effects.

Second, the direction of peak brightness rarely coincides with the subsolar direction. Across seasons and geometries, the azimuthal maximum is often offset by tens of degrees and can evolve substantially over a single comet rotation. The two best-covered intervals, 27 June 2015 (described in subsection 3.1) and 1 July 2015 (described in subsection 3.1), exhibit distinct behaviors: an abrupt flip from negative to positive offsets in the former, and a smooth, monotonic sweep across subsolar longitude in the latter. In both cases, the dominant peak tracks which large-scale surface elements (neck, head, foot) are illuminated and visible, rather than simply following the instantaneous subsolar direction.

Third, these different offset patterns are best explained by observational geometry rather than different insolation regimes because they occure on diurnal timescales. Specifically sub-spacecraft latitude and the changing visibility of concave/convex regions of the comet seem to drive these patterns. In other words, the nucleus's bilobate shape and self-occultations strongly impact what the instrument registers in its field of view, and thus the apparent main peak direction, even under nearly identical phase angles. This geometric control helps reconcile why the same active regions can yield abrupt flips in one epoch and smooth transitions in another. Together with the persistent mismatch between the peak and the subsolar point, this argues that nucleus shape, source regions with different strength of activity, and finite thermal response are essential to interpreting azimuthal profiles.

These conclusions rest on a sampling distance deliberately chosen near the onset

of free-radial outflow behavior identified in earlier OSIRIS analyses (Gerig et al., 2018; Tubiana et al., 2015) etc . By operating at projected distance of 10 km from the nucleus center and integrating narrowly in radius, we emphasized directional contrasts while remaining close to the regime where brightness approximates projected column density — a compromise that made the trends interpretable across many epochs without heavy modeling.

Next steps in this project would be to quantify secondary (minor) peaks in the azimuthal profiles and test their persistence across a full comet rotation. Practically, this can be done by applying a Savitzky–Golay (SG) smoothing filter to the azimuthal intensity distributions to suppress high-frequency noise while preserving peak shape, followed by a peak-finding stage based on prominence/width thresholds. On the Figure 14 you can see the implementation of this idea with locating and categorizing primary and secondary peaks into sectors of azymuthal profile. Labeling peaks consistently frame-to-frame would enable tracking their dwell time above threshold, angular drift rates, and recurrence at specific local times, clarifying whether they reflect stable source regions, transient activity, or effects of observational geometry.

Given the visible asymmetry between the dawn and dusk sectors (Figure 14), it would also be informative to define a dawn-to-dusk intensity ratio at fixed radial bounds and examine its dependence on observational geometry (phase angle, sub-spacecraft latitude/longitude) and season (pre- vs. post-perihelion). Analyzing how minor-peak statistics and the dawn–dusk ratio evolve over time, we can make conclusions about thermal effects.

Other extensions to this work may include: (i) expanding beyond Vis-610 to include NAC Orange and other continuum filters to check wavelength-dependent behavior; (ii) relaxing the phase-angle window in a controlled way to expand the available dataset with more STPs with dense rotational coverage to further disambiguate geometry vs. activity; (iii) overlaping the images with shape model and coordinate grid from Rosetta's SPICE kernel to link peaks to regional activity sources more precisely; and (iv) assimilating ROSINA/VIRTIS/MIRO/ GIADA constraints to break degeneracies between illumination, composition, and dust dynamics. Such an integrated program would turn the empirical patterns identified here into quantitative constraints on source localization, dust-to-gas coupling, and diurnal/seasonal evolution.

Going forward, combining how brightness peaks move in different image planes into a basic 3-D map of the inner coma can link surface sources to the large-scale coma patterns seen from Earth. The inner coma is the best proxy for the surface because it keeps fine structure and is only weakly changed by chemistry or secondary gas from icy grains. When surface images and inner-coma data are available at the same time, we can align peaks with specific terrains. Using these constraints, and carrying them outward with flow models (e.g., kinematic or DSMC-based), we can predict the fans and asymmetries that ground-based telescopes measure. This inside-to-outside mapping would let long-term Earth observations track regional activity in the many years between rare spacecraft missions.

In summary, this thesis demonstrates that even in the near-nucleus coma and under controlled geometry, 67P's dayside dominance coexists with strong directional structure that does not simply track the subsolar direction. The measured DS:NS behavior, the prevalence and evolution of peak offsets, and the decisive role of observation geometry provide a coherent empirical picture, that together with the set of curated and

reproducible diagnostics methods is ready to be fused with forward models. Together they highlight how nucleus shape and viewing geometry mediate what we observe, and they lay a practical foundation for turning rich OSIRIS image archives into physically grounded maps of cometary activity.

References

Attree, N., Schuckart, C., Bischoff, D., Gundlach, B., and Blum, J. (2024). Localized ejection of dust and chunks on comet 67p/churyumov–gerasimenko: testing how comets work. *Monthly Notices of the Royal Astronomical Society*, 535:65–77.

Balsiger, H., Altwegg, K., Bochsler, P., Eberhardt, P., Fischer, J., Graf, S., Jäckel, A., Kopp, E., Langer, U., Mildner, M., Müller, J., Riesen, T., Rubin, M., Scherer, S., Wurz, P., Wüthrich, S., Arijs, E., Delanoye, S., de Keyser, J., Neefs, E., Nevejans, D., Rème, H., Aoustin, C., Mazelle, C., Médale, J.-L., Sauvaud, J. A., Berthelier, J.-J., Bertaux, J.-L., Duvet, L., Illiano, J.-M., Fuselier, S. A., Ghielmetti, A. G., Magoncelli, T., Shelley, E. G., Korth, A., Heerlein, K., Lauche, H., Livi, S., Loose, A., Mall, U., Wilken, B., Gliem, F., Fiethe, B., Gombosi, T. I., Block, B., Carignan, G. R., Fisk, L. A., Waite, J. H., Young, D. T., and Wollnik, H. (2007). Rosina: Rosetta orbiter spectrometer for ion and neutral analysis. *Space Science Reviews*, 128:745–801.

Bertini, I., La Forgia, F., Fulle, M., Tubiana, C., Güttler, C., Moreno, F., Agarwal, J., Muñoz, O., Mottola, S., and Ivanovsky, S. (2019). The backscattering ratio of comet 67p/churyumov–gerasimenko dust coma as seen by osiris onboard rosetta. *Monthly Notices of the Royal Astronomical Society*, 482(3):2924–2933.

Choukroun, M., Altwegg, K., Kührt, E., Biver, N., Bockelée-Morvan, D., Drażkowska, J., Hérique, A., Hilchenbach, M., Marschall, R., Pätzold, M., Taylor, M. G. G. T., and Thomas, N. (2020). Dust-to-gas and refractory-to-ice mass ratios of comet 67p/churyumov-gerasimenko from rosetta observations. *Space Science Reviews*, 216(4):44.

Colangeli, L., Lopez-Moreno, J. J., Palumbo, P., Rodriguez, J., Cosi, M., Della Corte, V., Esposito, F., Fulle, M., Herranz, M., Jeronimo, J. M., Lopez-Jimenez, A., Epifani, E. M., Morales, R., Moreno, F., Palomba, E., and Rotundi, A. (2007). The grain impact analyser and dust accumulator (giada) experiment for the rosetta mission: design, performances and first results. *Space Science Reviews*, 128:803–821.

Coradini, A., Capaccioni, F., Drossart, P., Arnold, G., Ammannito, E., Angrilli, F., Barucci, A., Bellucci, G., Benkhoff, J., Bianchini, G., Bibring, J.-P., Blecka, M., Bockelée-Morvan, D., Capria, M. T., Carlson, R., Carsenty, U., Cerroni, P., Colangeli, L., Combes, M., Combi, M., Crovisier, J., De Sanctis, M. C., Encrenaz, E. T., Erard, S., Federico, C., Filacchione, G., Fink, U., Fonti, S., Formisano, V., Ip, W.-H., Jaumann, R., Kuehrt, E., Langevin, Y., Magni, G., McCord, T., Mennella, V., Mottola, S., Neukum, G., Palumbo, P., Piccioni, G., Rauer, H., Saggin, B., Schmitt, B., Tiphene, D., and Tozzi, G. (2007). Virtis: An imaging spectrometer for the rosetta mission. *Space Science Reviews*, 128:529–559.

de Niem, D., Kührt, E., Hviid, S., and Davidsson, B. (2018). Low velocity collisions of porous planetesimals in the early solar system. *Icarus*, 301:196–218.

Deller, J. (2020). *OSIRIS Science User Guide*, issue 2, revision e edition.

ESA (2014). Getting to know rosetta's comet. Accessed: 17 August 2025.

Filacchione, G., Groussin, O., Herny, C., Kappel, D., Mottola, S., Oklay, N., Pommerol, A., Wright, I., Yoldi, Z., Ciarniello, M., Moroz, L., and Raponi, A. (2019). Comet 67p/cg nucleus composition and comparison to other comets. *Space Science Reviews*, 215(1):19.

Gerig, S.-B., Marschall, R., Thomas, N., Bertini, I., Bodewits, D., Davidsson, B., Fulle, M., Ip, W.-H., Keller, H. U., Küppers, M., Preusker, F., Scholten, F., Su, C. C., Toth, I., Tubiana, C., Wu, J.-S., Sierks, H., Barbieri, C., Lamy, P. L., Rodrigo, R., Koschny, D., Rickman, H., Agarwal, J., Barucci, M. A., Bertaux, J.-L., Cremonese, G., Da Deppo, V., Debei, S., De Cecco, M., Deller, J., Fornasier, S., Groussin, O., Gutiérrez, P. J., Güttler, C., Hviid, S. F., Jorda, L., Knollenberg, J., Kramm, J. R., Kührt, E., Lara, L. M., Lazzarin, M., Lopez Moreno, J. J., Marzari, F., Mottola, S., Naletto, G., Oklay, N., and Vincent, J.-B. (2018). On deviations from free-radial outflow in the inner coma of comet 67p/churyumov–gerasimenko. *Icarus*, 311:1–22.

Gerig, S.-B., Pinzón-Rodríguez, O., Marschall, R., Wu, J.-S., and Thomas, N. (2021). Dayside-to-nightside dust coma brightness asymmetry and its implications for night-side activity at comet 67p/churyumov–gerasimenko. *Icarus*, 361:114378.

Glassmeier, K.-H., Boehnhardt, H., Koschny, D., Kührt, E., and Richter, I. (2007). The rosetta mission: Flying towards the origin of the solar system. *Space Science Reviews*, 128:1–21.

Gulkis, S., Frerking, M., Crovisier, J., Beaudin, G., Hartogh, P., Encrenaz, P., Koch, T., Kahn, C., Salinas, Y., Nowicki, R., Irigoyen, R., Janssen, M., Stek, P., Hofstadter, M., Allen, M., Backus, C., Kamp, L., Jarchow, C., Steinmetz, E., Deschamps, A., Krieg, J., Gheudin, M., Bockelée-Morvan, D., Biver, N., Encrenaz, T., Despois, D., Ip, W., Lellouch, E., Mann, I., Muhleman, D., Rauer, H., Schloerb, P., and Spilker, T. (2007). Miro: Microwave instrument for the rosetta orbiter. *Space Science Reviews*, 128:561–597.

Hughes, D. W. (1975). Cometary outbursts, a brief survey. *Quarterly Journal of the Royal Astronomical Society*, 16:410.

Keller, H. U., Barbieri, C., Lamy, P., Rickman, H., Rodrigo, R., Wenzel, K. P., Sierks, H., A'Hearn, M. F., Angrilli, F., Barucci, M. A., Bertaux, J. L., Bianchini, G., Boit, J. L., Brown, V., Burns, J. A., Büttner, I., Castro, J. M., Cremonese, G., Curdt, W., Da Deppo, V., Debei, S., Cecco, M. D., Davidsson, B., Ebert, R., Fulle, M., Gaskell, R., Gliem, F., Guizzo, G. P., Hviid, S. F., Ip, W. H., Jorda, L., Koschny, D., Kramm, J. R., Kührt, E., Küppers, M., Lara, L. M., Llebaria, A., Loques, F., López, A., López-Jimenez, A., Meller, R., Michalik, H., Michelena, M. D., Müller, R., Naletto, G., Origné, A., Parzianello, G., Pertile, M., Quintana, C., Ragazzoni, R., Ramous, P., Reiche, K. U., Reina, M., Rodríguez, J., Rousset, G., Sabau, L., Sanz, A., Sivan, J. P., Stöckner, K., Tabero, J., Telljohann, U., Thomas, N., Timon, V., Tiphène, D., Tomasch, G., Wirth, K., Zaccariotto, M., and Pérez, J. L. (2007). OSIRIS – the scientific camera system onboard rosetta. *Space Science Reviews*, 128(1-4):433–506.

Keller, H. U., Mottola, S., et al. (2015). Insolation, erosion, and morphology of comet 67P/Churyumov-Gerasimenko. *Astronomy Astrophysics*, 583:A34.

Kissel, J., Altwegg, K., Clark, B. C., Colangeli, L., Cottin, H., Czempiel, S., Eibl, J., Engrand, C., Fehringer, H. M., Feuerbacher, B., Fomenkova, M., Glasmachers, A., Greenberg, J. M., Grün, E., Haerendel, G., Henkel, H., Hilchenbach, M., von Hoerner, H., Höfner, H., Hornung, K., Jessberger, E. K., Koch, A., Krüger, H., Langevin, Y., Parigger, P., Raulin, F., Rüdenauer, F., Rynö, J., Schmid, E. R., Schulz, R., Silén, J., Steiger, W., Stephan, T., Thirkell, L., Thomas, R., Torkar, K., Utterback, N. G., Varmuza, K., Wanczek, K. P., Werther, W., and Zscheeg, H. (2007). Cosima: High resolution time-of-flight secondary ion mass spectrometer for the analysis of cometary dust particles onboard rosetta. *Space Science Reviews*, 128:823–867.

Kramer, T., Läuter, M., Rubin, M., and Altwegg, K. (2017). Outgassing of comet 67P/Churyumov-Gerasimenko near perihelion: A forward modeling approach. *Monthly Notices of the Royal Astronomical Society*, 469:S20–S28.

Kramer, T. and Noack, M. (2016). On the origin of inner coma structures observed by rosetta during a diurnal rotation of comet 67p/churyumov–gerasimenko. *The Astrophysical Journal Letters*, 823(1):L11.

Le Roy, L., Altwegg, K., Balsiger, H., Berthelier, J.-J., Bieler, A., Briois, C., Calmonte, U., Combi, M. R., De Keyser, J., Dhooghe, F., Fiethe, B., Fuselier, S. A., Gasc, S., Gombosi, T. I., Hässig, M., Jäckel, A., Rubin, M., and Tzou, C.-Y. (2015). Inventory of the volatiles on comet 67P/Churyumov-Gerasimenko from Rosetta/ROSINA. *Astronomy & Astrophysics*, 583:A1.

Marschall, R., Markkanen, J., Gerig, S.-B., Pinzón-Rodríguez, O., Thomas, N., and Wu, J.-S. (2020a). The dust-to-gas ratio, size distribution, and dust fall-back fraction of comet 67p/churyumov-gerasimenko: Inferences from linking the optical and dynamical properties of the inner comae. *Frontiers in Physics*, 8:227.

Marschall, R., Mottola, S., Su, C. C., et al. (2017). Cliffs versus plains: Can rosina/cops and osiris data of comet 67p/churyumov–gerasimenko in autumn 2014 constrain inhomogeneous outgassing? *Astronomy & Astrophysics*, 605:A112.

Marschall, R., Skorov, Y. V., Zakharov, V., Rezac, L., Gerig, S.-B., Christou, C., Dadzie, S. K., Migliorini, A., Rinaldi, G., Agarwal, J., Vincent, J.-B., and Kappel, D. (2020b). Cometary comae-surface links: The physics of gas and dust from the surface to a spacecraft. *Space Science Reviews*, 216(8):130.

Marschall, R., Su, C. C., Liao, Y., Thomas, N., Altwegg, K., Sierks, H., Ip, W.-H., Keller, H. U., Knollenberg, J., Kührt, E., Lai, I. L., Rubin, M., Skorov, Y., Wu, J. S., Jorda, L., Preusker, F., Scholten, F., Gracia-Berná, A., Gicquel, A., Naletto, G., Shi, X., and Vincent, J.-B. (2016). Modelling observations of the inner gas and dust coma of comet 67P/Churyumov-Gerasimenko using ROSINA/COPS and OSIRIS data: First results. *Astronomy & Astrophysics*, 589:A90.

Mumma, M. J. and Charnley, S. B. (2011). The chemical composition of comets—emerging taxonomies and natal heritage. *Annual Review of Astronomy and Astrophysics*, 49:471–524.

Oklay, N. (2015). Characterization of OSIRIS NAC filters for the interpretation of multispectral data of comet 67P/Churyumov-Gerasimenko. *Astronomy & Astrophysics*, 583:A45.

Pätzold, M., Andert, T. P., Hahn, M., Barriot, J. P., Asmar, S. W., Häusler, B., et al. (2019). The nucleus of comet 67p/churyumov-gerasimenko – part i: the global view – nucleus mass, mass-loss, porosity, and implications. *Monthly Notices of the Royal Astronomical Society*, 483:2337–2346.

Riedler, W., Torkar, K., Jeszenszky, H., Romstedt, J., Alleyne, H. S. C., Arends, H., Barth, W., van der Biezen, J., Butler, B., Ehrenfreund, P., Fehringer, M., Fremuth, G., Gavira, J., Havnes, O., Jessberger, E. K., Kassing, R., Klöck, W., Koeberl, C., Levasseur-Regourd, A. C., Maurette, M., Rüdenauer, F., Schmidt, R., Stangl, G., Steller, M., and Weber, I. (2007). Midas: The micro-imaging dust analysis system for the rosetta mission. *Space Science Reviews*, 128:869–904.

Sekanina, Z. (1987). Anisotropic emission from comets: fans versus jets. i. concept and modelling. In *Dynamical Problems in Cometary Science*, volume SP-278 of *ESA Special Publication*, pages 315–322, Noordwijk, The Netherlands. European Space Agency.

Shi, X., Hu, X., Mottola, S., et al. (2018). Coma morphology of comet 67P controlled by insolation over irregular nucleus. *Nature Astronomy*, 2:562–567.

Skorov, Y. and Blum, J. (2012). Dust release and tensile strength of the non-volatile layer of cometary nuclei. *Icarus*, 221:1–11.

Stern, S. A., Slater, D. C., Scherrer, J., Stone, J., Versteeg, M., A'Hearn, M. F., Bertaux, J. L., Feldman, P. D., Festou, M. C., Parker, J. W., and Siegmund, O. H. W. (2007). Alice: the rosetta ultraviolet imaging spectrograph. *Space Science Reviews*, 128:507–527.

Taylor, M. G. G. T., Altobelli, N., Buratti, B. J., and Choukroun, M. (2017). The rosetta mission orbiter science overview: the comet phase. *Philosophical Transactions of the Royal Society A: Mathematical, Physical and Engineering Sciences*, 375(2097):20160262.

Tubiana, C., Fornasier, S., Hasselmann, P. H., Barucci, M. A., Sierks, H., Barbieri, C., Lamy, P., Rickman, H., Rodrigo, R., and Wenzel, K. P. (2015). Scientific assessment of the quality of osiris images. *Planetary and Space Science*, 111:80–85.

Tubiana, C., Rinaldi, G., Güttler, C., Snodgrass, C., Shi, X., Hu, X., Marschall, R., Fulle, M., Bockelée-Morvan, D., Naletto, G., Capaccioni, F., Sierks, H., Arnold, G., Barucci, M. A., Bertaux, J.-L., Bertini, I., Bodewits, D., Capria, M. T., Ciarniello, M., Cremonese, G., Crovisier, J., Da Deppo, V., Debei, S., De Cecco, M., Deller, J., De Sanctis, M. C., Davidsson, B., Doose, L., Erard, S., Filacchione, G., Fink, U., Formisano, M., Fornasier, S., Gutiérrez, P. J., Ip, W.-H., Ivanovski, S., Kappel, D., Keller, H. U., Kolokolova, L., Koschny, D., Krüger, H., La Forgia, F., Lamy, P. L., Lara, L. M., Lazzarin, M., Levasseur-Regourd, A. C., Lin, Z.-Y., Longobardo, A., López-Moreno, J. J., Marzari, F., Migliorini, A., Mottola, S., Rodrigo, R., Taylor,

F., Tóth, I., and Zakharov, V. (2019). Diurnal variation of dust and gas production in comet 67p/churyumov-gerasimenko at the inbound equinox as seen by osiris and virtis-m on board rosetta. *Astronomy & Astrophysics*, 632:A1.

Vincent, J.-B., A'Hearn, M. F., Lin, Z.-Y., et al. (2016a). Summer fireworks on comet 67P: A season of outbursts. *Monthly Notices of the Royal Astronomical Society*, 462:S184–S194.

Vincent, J.-B., Oklay, N., Pajola, M., et al. (2016b). Are fractured cliffs the source of cometary dust jets? insights from osiris/rosetta at 67p/churyumov–gerasimenko. *Astronomy & Astrophysics*, 587:A14.

Whipple, F. L. (1950). A Comet Model. I. The Acceleration of Comet Encke. *The Astrophysical Journal*, 111:375–394.

Whipple, F. L. (1986). The cometary nucleus: Current concepts. In *Proceedings of the 20th ESLAB Symposium on the Exploration of Halley's Comet. Volume 2: Dust and Nucleus*, volume SP-250 of *ESA Special Publication*, pages 281–288, Noordwijk, The Netherlands. ESA.

Zakharov, V. V., Ivanovski, S. L., Crifo, J.-F., et al. (2018). A study of the dust environment of comet 67P/Churyumov-Gerasimenko based on a multi-fluid approach. *Icarus*, 312:121–131.